Article

Covalent Proximity Scanning of a Distal Cysteine to Target PI3Kα

Chiara Borsari,[#] Erhan Keles,[#] Jacob A. McPhail, Alexander Schaefer, Rohitha Sriramaratnam, Wojciech Goch, Thorsten Schaefer, Martina De Pascale, Wojciech Bal, Matthias Gstaiger, John E. Burke, and Matthias P. Wymann*

Read Online

ACCESS | Metrics & More | Article Recommendations | Supporting Information

ABSTRACT: Covalent protein kinase inhibitors exploit currently noncatalytic cysteines in the adenosine 5′-triphosphate (ATP)-binding site via electrophiles directly appended to a reversible-inhibitor scaffold. Here, we delineate a path to target solvent-exposed cysteines at a distance >10 Å from an ATP-site-directed core module and produce potent covalent phosphoinositide 3-kinase α (PI3Kα) inhibitors. First, reactive warheads are used to reach out to Cys862 on PI3Kα, and second, enones are replaced with druglike warheads while linkers are optimized. The systematic investigation of intrinsic warhead reactivity (k_{chem}), rate of covalent bond formation and proximity (k_{inact} and reaction space volume V_r), and integration of structure data, kinetic and structural modeling, led to the guided identification of high-quality, covalent chemical probes. A novel

$$\frac{k_{inact}}{K_i} = k_{cat} = \frac{1}{\sigma} \cdot \frac{k_{chem}}{K_i \cdot N_A \cdot V_r}$$

stochastic approach provided direct access to the calculation of overall reaction rates as a function of k_{chem}, k_{inact}, K_i, and V_r, which was validated with compounds with varied linker lengths. X-ray crystallography, protein mass spectrometry (MS), and NanoBRET assays confirmed covalent bond formation of the acrylamide warhead and Cys862. In rat liver microsomes, compounds **19** and **22** outperformed the rapidly metabolized CNX-1351, the only known PI3Kα irreversible inhibitor. Washout experiments in cancer cell lines with mutated, constitutively activated PI3Kα showed a long-lasting inhibition of PI3Kα. In SKOV3 cells, compounds **19** and **22** revealed PI3Kβ-dependent signaling, which was sensitive to TGX221. Compounds **19** and **22** thus qualify as specific chemical probes to explore PI3Kα-selective signaling branches. The proposed approach is generally suited to develop covalent tools targeting distal, unexplored Cys residues in biologically active enzymes.
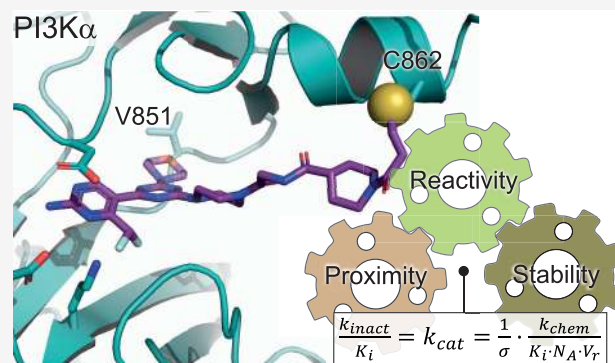
INTRODUCTION

Eight covalent kinase inhibitors, afatinib,[1] ibrutinib,[2] osimertinib,[3] neratinib,[4] dacomitinib,[5] acalabrutinib,[6] zanubrutinib,[7] and mobocertinib,[8,9] have been approved by the Food and Drug Administration (FDA) as anticancer agents to date. This renewed the interest in targeted covalent inhibitors (TCIs). Advantages of irreversible inhibitors include increased ligand efficiency, specificity, and prolonged duration of action.[10] Besides therapeutic approaches, TCIs find application as chemical probes to explore the role of kinases in the onset of human disease.[11] Currently, only a limited number of signaling proteins' cysteines have been successfully targeted.[12,13] TCIs are usually generated using a reversible-inhibitor scaffold with a high affinity for the primary target, which is then extended by an electrophilic, reactive functional group. Often dubbed warhead, these electrophiles engage in a Michael addition to form a covalent link with the target cysteine. This strategy has been successfully exploited to target protein kinases, including Bruton's tyrosine kinase (BTK)[2,14] and epidermal growth factor receptor (EGFR)[15] (Figure 1a,c). The incorporation of an electrophile on PCI-29732 and gefitinib scaffolds yielded the cysteine-targeting covalent inhibitors acalabrutinib and ibrutinib

for BTK (Figure 1b), and dacomitinib and afatinib for EGFR (Figure 1d). Typically, highly reactive warheads in covalent drugs lead to toxicity and off-target reactions with cellular nucleophiles such as thiols, including glutathione (GSH). Sadly, even for marketed drugs like ibrutinib, clear structure–activity relationship (SAR) studies leading to compound selection are obscured.[2] The intrinsic reactivity with thiols has not been determined for recent covalent inhibitors,[16−19] even though a variety of warheads have been explored.[7,20] Besides warhead reactivity, the optimization of warhead proximity is often not considered in the generation of covalent probes.[21] Most of the explored targeted cysteines are in close proximity to the reversible scaffold,[22] and structural analysis of the linker has not been examined or disclosed. Targeting of remote cysteines

Journal of the American Chemical Society
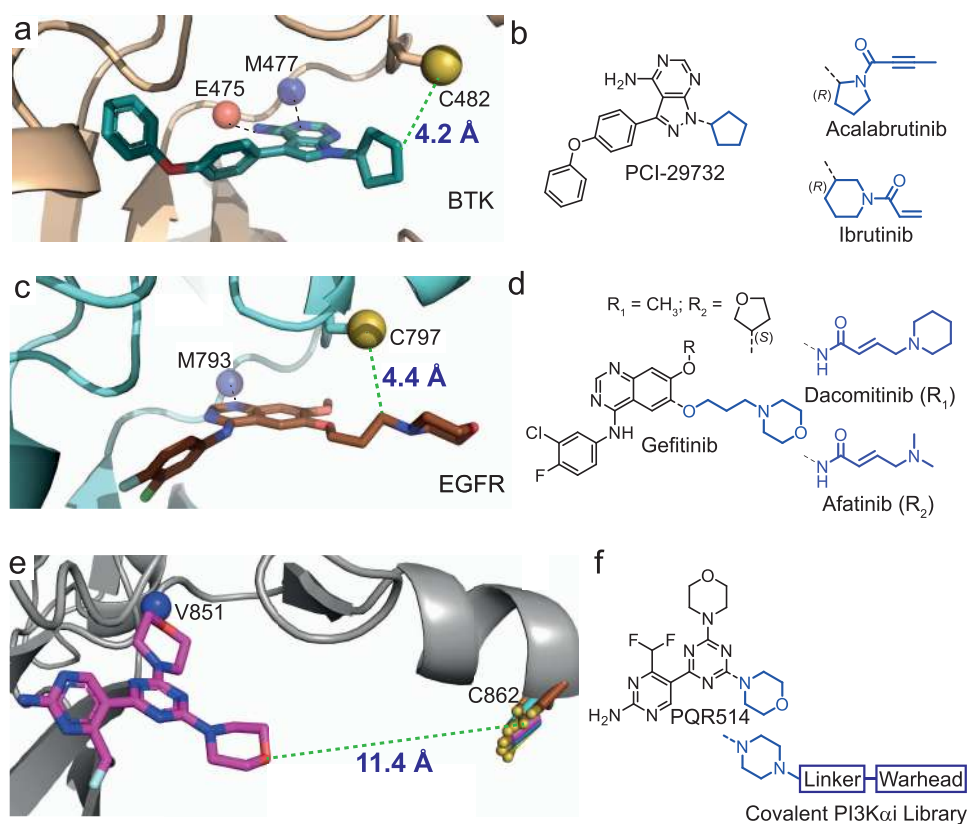pubs.acs.org/JACS
Article

Figure 1. (a, c) Design strategy for the development of irreversible inhibitors targeting (a) BTK and (c) EGFR. X-ray crystallographic structure of (a) BTK (colored wheat) in complex with PCI-29732 (teal; PDB ID 3GEN)[78] and (c) EGFR (cyan) in complex with gefitinib (brown, PDB ID 4I22).[79] (b, d) Chemical structure of the reversible-inhibitor scaffolds and covalent derivatives are depicted. The incorporation of the warhead on PCI-29732 led to acabrutinib and ibrutinib, and gefitinib served as a scaffold for dacomitinib and afatinib. (e) PQR514[46] (magenta) bound to phosphoinositide 3-kinase α (PI3Kα) (gray; based on PDB ID 6OAC[59]). Cys862 positions from eight superimposed PI3Kα-inhibitor complexes are shown (see Table S1 for details). The position of the cysteine thiols (yellow) is conserved across the different complexes and deviates less than 2.6 Å. (f) Schematic design of the covalent PI3Kαi library. The distances between reversible inhibitor skeletons and the targeted nucleophiles are shown as dashed green lines ($\sim$4 Å for BTK and EGFR vs $\sim$11 Å for PI3Kα).

has been rarely approached, but a few examples are present in the literature, including anaplastic lymphoma kinase (Alk),[23] cyclin-dependent kinases 12 and 13 (CDK12 and CDK13),[24,25] and CDK7[26] covalent inhibitors.

CNX-1351 is the only known covalent inhibitor of phosphoinositide 3-kinase α (PI3Kα) and targets its remote Cys862,[27] which is not conserved in other PI3Ks. CNX-1351 shows a relatively poor in vitro and cellular potency, and its chemical features and warhead do not make it suitable for a lead optimization process.

Thus, a rational path to the identification of highly selective, covalent druglike inhibitors is currently elusive. A systematic study of reactivity, proximity, and the integration of chemical and biochemical measurements, paired with kinetic and structural modeling, is required for the design of high-quality covalent chemical probes.

Herein, we have selected PI3Kα to outline a roadmap to target solvent-exposed cysteines at >10 Å from a reversible binding core module. The PI3K signaling pathway plays a key role in human carcinogenesis, and the PI3K family is divided into three classes according to sequence homology and substrate specificity.[28,29] The class I PI3K family consists of four isoforms (PI3Kα, β, δ, and γ). The genetic locus encoding PI3Kα, *PIK3CA*, is frequently mutated and implicated in tumor progression.[30,31] Structurally diverse, reversible pan-class I PI3K inhibitors (PI3Ki) are currently evaluated in clinical trials,

either as monotherapy, or as part of combination regimens.[32–34] Alpelisib (BYL719)[35] has been approved in combination with Fulvestrant for the treatment of HR+/HER2− advanced breast cancer bearing activating mutations in *PIK3CA*.[36–39] BYL719 shows biochemical selectivity for PI3Kα,[35] but is not sufficiently isoform-selective to serve as a chemical probe to dissect specifically PI3Kα-dependent biological processes. However, BYL719's preference for PI3Kα enlarges its therapeutic window in *PIK3CA*-mutant tumors[40] and makes it suitable to treat *PIK3CA*-related overgrowth syndrome (PROS).[41] Targeting the PI3Kα-specific Cys862 with covalent inhibitors provides a strategy to achieve exquisite PI3K isoform selectivity and to generate tools to elucidate the role of PI3Kα in cancer and metabolism. Here, a rational path to covalent inhibitors targeting distal cysteines is depicted, which is driven by a stepwise adaptation of warhead reactivity and proximity, supervised by a rigorous determination of chemical and enzymatic reactivities validating the proximity to the targeted nucleophile. The approach is generally suited to target unexplored Cys residues in biologically active enzymes.

■ RESULTS AND DISCUSSION

Design of Covalent PI3Kα Inhibitors. Starting from the clinical candidate PQR309,[42–45] we have previously identified the preclinical candidate PQR514 with improved, low nanomolar affinity for PI3Kα (K_i for PI3Kα = 2.2 nM[46]). The
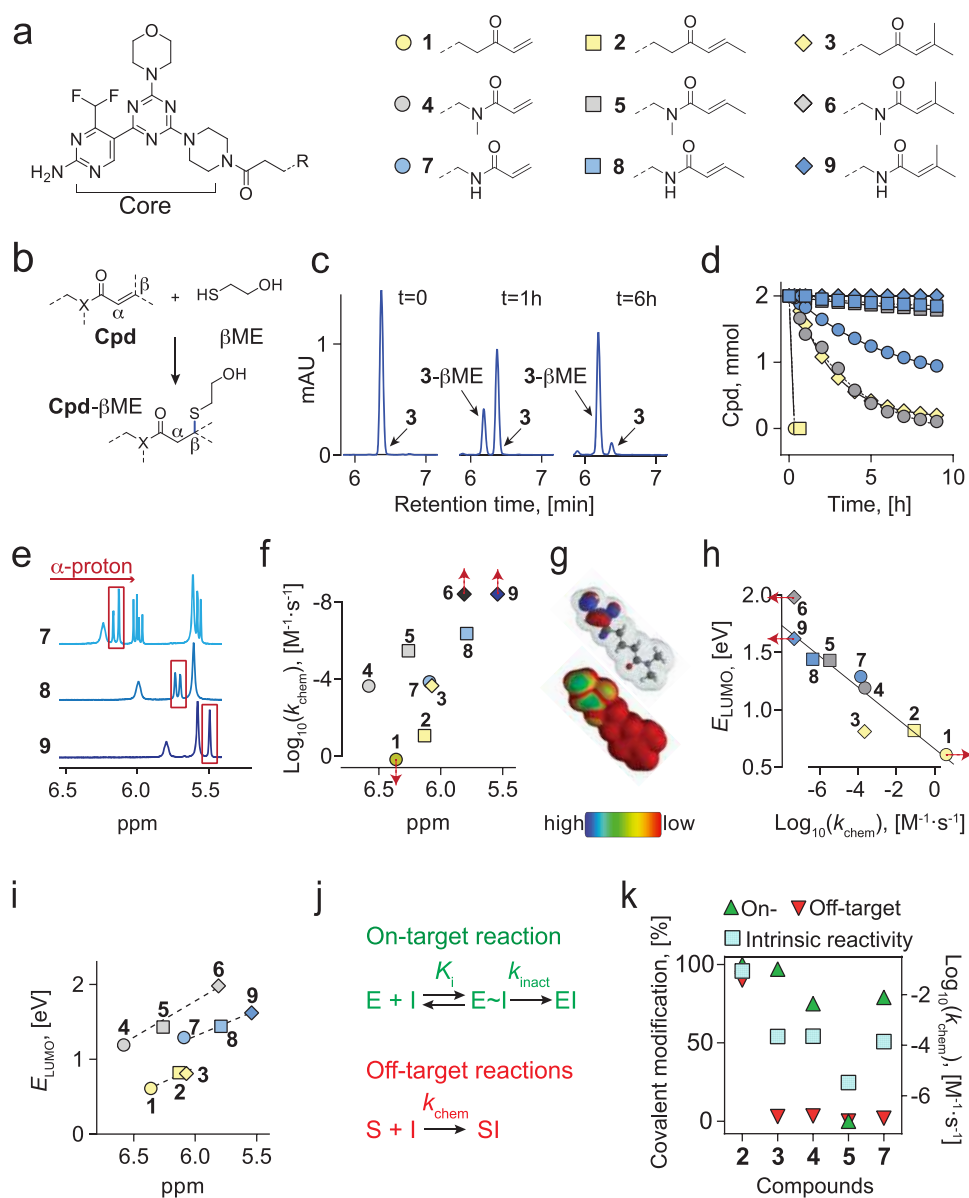
Figure 2. (a) Chemical structure of a set of nine warhead-containing compounds (**1–9**). (b) General reaction of warhead-containing compounds with βME. (c) High-performance liquid chromatography (HPLC) reaction monitoring of inhibitor (**3**) and its βME adduct (**3**-βME) formation. (d) Time-dependent inhibitor consumption curves used to calculate k_{chem}. Values are mean ± standard deviation (SD) ($n = 3$). Error bars are not shown when smaller than symbols. (e) Chemical shift of the α-proton in ^{1}H NMR spectra of compounds bearing an unsubstituted double bond (**7**) and β-methyl (**8**)- and β,β-dimethyl (**9**)-substituted warheads. (f) Intrinsic reactivity of the inhibitors (k_{chem}) plotted against the chemical shift of the α-protons of the indicated compounds. Raw data and details for k_{chem} calculations are reported in Table S2 and in the Materials and Methods section in the Supporting Information. The second-order rate constant k_{chem} could not be measured for compounds **6** and **9** due to lack of reactivity with 12 M βME, and also not for **1** due to its extremely fast reaction with 1 mM βME. k_{chem} for compound **8** was lower than 1×10^{-6} M^{-1} s^{-1} and was thus considered nonreactive. These three values are therefore "out-off scale" (denoted with red arrows) for k_{chem}. (g) Representation of energy of the lowest-unoccupied molecular orbital (LUMO) electron density (top) and LUMO map (bottom) for compound **1**. Electron deficiency ranges from blue (high) to red (low). Given that the LUMO designates space available for a pair of electrons, color tints toward blue in the LUMO map indicate where a nucleophilic attack would likely occur. Calculations were performed using Spartan 18, Wavefunction, Inc. (h) E_{LUMO} values plotted against the intrinsic reactivity of the inhibitors (k_{chem}). Raw data and details for k_{chem} calculations are reported in Table S2 and in the Materials and Methods section in the Supporting Information. As in (f), values for k_{chem} denoted with red arrows are "out-off scale". (i) Chemical shift of α-protons of indicated compounds plotted against E_{LUMO} values. (j) Model for cellular on- and off-target reactions of covalent inhibitors. In the on-target reaction (green), enzyme E and inhibitor I form first a reversible E~I complex (equilibrium dependent on K_i), which is then converted to a covalent EI complex (controlled by k_{inact}). Competing off-target reactions (red) with cellular sulfhydryls (S) consume the inhibitor and form a stable SI adduct. (k) On- and off-target covalent reactions of inhibitors as depicted in (j) were modeled using KinTek Global Kinetic Explorer: concentrations were set to 7 mM for intracellular sulfhydryls (for intracellular reduced glutathione (GSH) concentrations, see ref 80); for the targeted enzyme (PI3Kα) to 10 nM; and for indicated covalent inhibitors to 100 nM. Experimental values for k_{inact} and k_{chem} used for the modeling are listed in Table S2 and Figure S1. Details for the determination of k_{inact} are given in Figure 3 and associated materials.
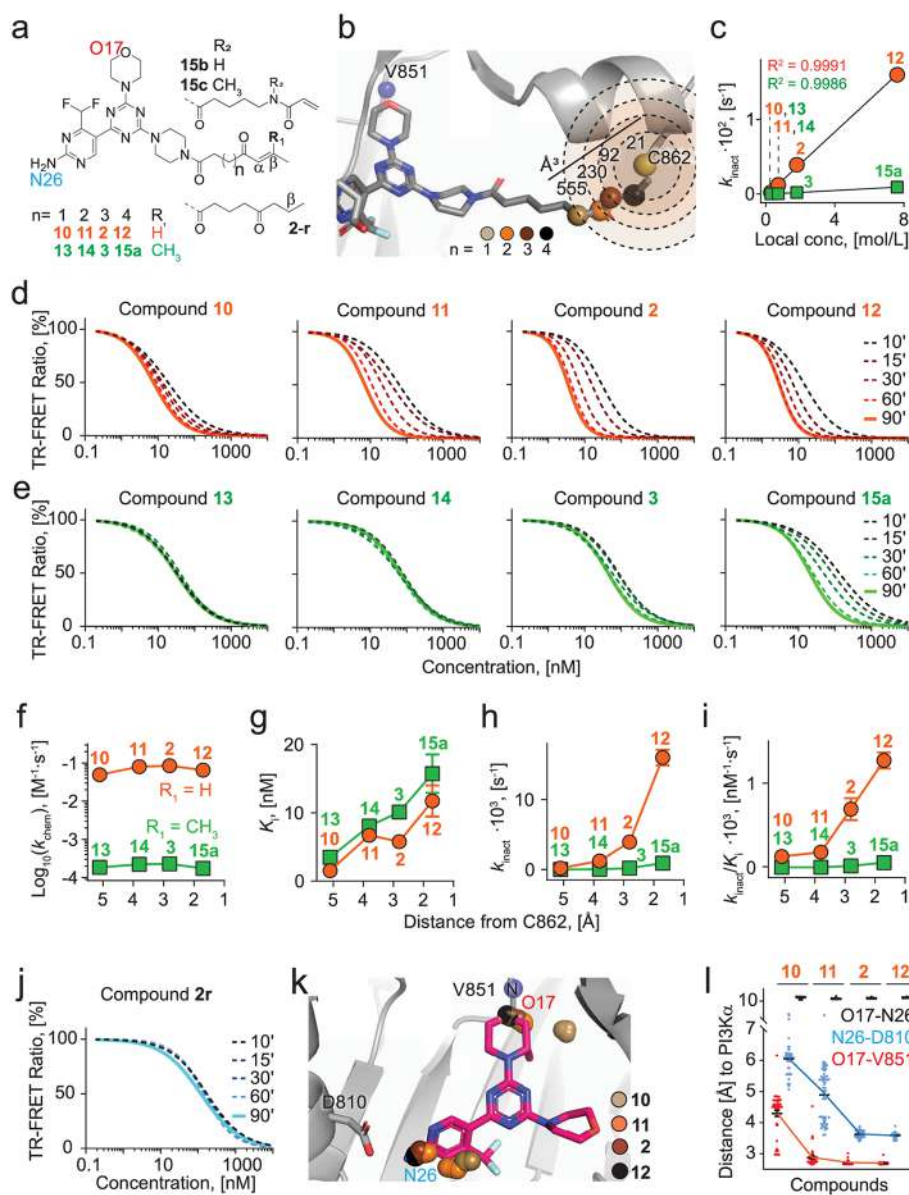
Figure 3. (a) Chemical structure of a collection of nine compounds with pairwise matched linkers and either fast (**2**, **10−12**) or moderately (**3**, **13−15a**) reactive Michael acceptors, and of **15b** and **15c**. (b) The reactive volume (V_r) of the warhead was estimated by a sphere around the sulfur atom of Cys862, with a radius equal to the distance (d) between the Cys862 sulfur and the β-carbon of the Michael acceptor ($V_r = 4/3 \cdot \pi \cdot d^3$); see Table S4 for values. The modeled locations of the β-carbon of the Michael acceptor are indicated by spheres colored as in (a). (c) Correlation between k_{inact} and the local warhead concentration (see Table S4 for calculation). (d, e) Time-dependent IC_{50} determinations derived from time- and concentration-dependent time-resolved fluorescence resonance energy transfer (TR-FRET) ratios curves depicted in Figure S2 (IC_{50}s for all compounds with error bars, see Figure S13). Strong (**2**, **10−12** (d)) and weak (**3**, **13−15a** (e)) electrophiles were investigated. (f) Compound-specific intrinsic reactivity (k_{chem}) determined as in Figure 2; (g) dissociation constants (K_i) calculated from concentration and time-dependent TR-FRET experiments as shown in Figure S2 (h) rate constants for covalent binding to PI3Kα (k_{inact}); (i) second-order rate constant used to characterize covalent binding of irreversible inhibitors to the target protein (k_{inact}/K_i). The calculation of kinetic parameters was carried out through global fitting for numerical integration to a kinetic model using KinTek Global Kinetic Explorer modeling software.[73−76,81,82] All values are shown as mean ± SD ($n = 3$). Error bars are not shown when smaller than the symbols. Orange, strong electrophiles; green, weak electrophiles. The distance between the Michael acceptor (β-carbon) and Cys862 thiol was calculated using PyMOL 2.3.5 Schrödinger, Inc. (see Figure S3 and Table S3). (j) TR-FRET experiments for the reversible analogue of compound **2** (**2r**). (k) Covalent docking of compounds **2**, **10−12** using CovDock Schrödinger. Representation of the shift of the morpholine oxygen (spheres, in hinge region defined by Val851) and of the NH_2 (spheres, in binding affinity region defined by Asp810) with respect to PQR530 scaffold (magenta) is displayed. (l) CovDock Schrödinger modeling has been used to investigate the displacement of the PI3K core module of the indicated compounds when covalently bound to Cys862 of PI3Kα. The distances of (i) the morpholine oxygen atom (O17) and the N nitrogen atom of Val851 backbone amide (O17-V851, red) in the hinge region, and (ii) the amino group (N26) of the aminopyrimidine and the closest oxygen atom in COO^- side chain of Asp810 (N26-D810, light blue) in the affinity region were determined from CovDock modeling coordinates from 50 predicted poses, and average and SD were calculated. As a control for a structural distortion of the PI3K-binding module, the distances between the O17 and N26 atoms (O17-N26, black) were determined. Numbering of inhibitor atoms can be found in (a) and (k). Distances are reported in angstrom. Modeling was performed using PDB ID 6OAC[59] as a starting point. All compounds are depicted in Figure S6.

PQR514 core was a suitable starting point to serve as PI3Kα-binding module. Cys862 in PI3Kα is located at ~11 Å from the solvent-exposed morpholine oxygen atom of PQR514 (Figure 1e). An overlay of eight PI3Kα-inhibitor crystal structures showed that the position and orientation of the Cys862 side chain were maintained across all structures (Figure 1e and Table S1), thus providing a fair estimate of the target space. Subsequently, a variety of warheads and linkers were studied to assess the required warhead reactivity and the spatial trajectory of the Michael acceptor (for a schematic setup, see Figure 1f).

Tuning of Warhead Reactivity. The control of warhead reactivity is a pivotal parameter in the development of covalent chemical probes and drug candidates. It has been reported that the rate of thiol-Michael addition to α,β-unsaturated carbonyls decreases from enones to acrylamides and that electron-donating groups and alkyl moieties reduce the rate of thiol addition due to electronic and steric effects.[47] Even though chemical and computational methods have been used to assess the half-life of warheads,[48] their intrinsic reactivity, as well as its correlation with the rate of covalent bond formation, is often neglected in SAR elucidation.

Up-to-date, several approaches have been applied to predict warhead reactivity, including NMR chemical shifts,[49] pK_a assessments,[50] and quantum mechanics/molecular mechanics (QM/MM).[51] ^{1}H and ^{13}C NMR have been previously used to predict the reactivity of structurally similar α,β-unsaturated carbonyls.[52] Experimentally, the half-life to adduct formation with GSH has served as a surrogate for measuring the relative reactivity of cysteine-targeting warheads,[53,54] and absolute rate constants (k_{GSH} or k_{chem}) have been systematically established for a collection of N-aryl[55] and N-phenyl[56] acrylamides. Here, we designed and synthesized PI3Kis bearing nine different warheads, including enones and acrylamides (1−9, Figure 2a).

We experimentally determined the rate constants of adduct formation of this diverse set of Michael acceptors with β-mercaptoethanol (βME; Figure 2b): the nine warhead-containing compounds (1 mM) were incubated with βME at a selected concentration from 1 mM to 12 M at 37 °C in phosphate-buffered saline (PBS, pH 7.4)/dimethyl sulfoxide (DMSO) mixtures (v/v 1:4). The temporal progress of the reactions was monitored by HLPC (Figure 2c) and βME adducts were confirmed by mass spectrometry (MS) (see the MALDI-MS Spectra of β-Mercaptoethanol Adducts section in the Supporting Information). The resulting time-dependent inhibitor consumption/adduct formation curves (Figure 2d) were fitted using pseudo-first-order reaction kinetics (yielding k'), and were used to calculate the second-order reaction rate constant (k_{chem}, Table S2). Second-order rate constants could not be reliably calculated for compounds 6 and 9 due to lack of reactivity with 12 M βME, and also not for 1 because of the extremely fast reaction with 1 mM βME. The presented set of Michael acceptors showed a broad range of reactivities spanning over 5 log units for k_{chem}.

As a predictive analytical parameter for k_{chem}, ^{1}H NMR chemical shifts of the alkene α-proton of the warheads were explored: relative to the unsubstituted double bond in 1, 4, 7, the signal of the alkene α-proton was shifted upfield in β-methyl (2, 5, 8)- and β,β-dimethyl (3, 6, 9)-substituted warheads (see, for example, compounds 7−9, Figure 2e). When Log(k_{chem}) values were, however, plotted against chemical shifts of the α position in ^{1}H NMR, no reliable correlation could be established (Figure 2f).

Subsequently, LUMO maps (Figure 2g) with the correspondent energies of lowest-unoccupied molecular orbitals (E_{LUMO}) were calculated. Low-energy LUMO makes chemical moieties reactive toward nucleophiles. As LUMO energies have been used to assess the electrophilicity of molecules, they could be predictive of k_{chem} values. A moderate correlation between E_{LUMO} energies and experimentally determined Log(k_{chem}) values was found ($R^2 = 0.68$, Figure 2h). Similarly, no fair correlation was obtained when E_{LUMO} values were plotted against the chemical shift of the α-proton ($R^2 = 0.34$, Figure 2i).

Altogether, these results highlight that a measurement of k_{chem} is essential for a systematic classification of warhead reactivity. To estimate on-target and off-target reactivity, the reaction of the warhead with Cys862 of PI3Kα or cellular thiols was modeled using KinTek software using the two competitive on-target and off-target reactions depicted in Figure 2j. The on-target model involves the inhibitor dissociation constant K_i for the formation of the reversible enzyme−inhibitor complex (E~I) and the rate of the covalent reaction with the protein (k_{inact}; for the measurement of K_i and k_{inact}, see next section) to form the irreversible inhibitor complex (EI).

The results of this modeling (Figures 2k and S1) illustrate that (i) highly reactive electrophiles (2) react very rapidly with the target, but are mostly consumed by off-target reactions; (ii) moderate electrophiles (3, 4, 7) selectively engage the target and show negligible side reactions; and (iii) minimally reactive molecules (5) engage neither the desired target nor undesired cellular thiols.

This defines a range for k_{chem} from ~5 × 10⁻⁵ to 5 × 10⁻³ M⁻¹·s⁻¹ for warheads with an acceptable off-target activity. On-target reactivity is, however, promoted by reversible affinity and warhead proximity to the targeted nucleophilic amino acid side chain.

While not suitable for drug development, we show below that highly electrophilic warheads (see 2) can be exploited in the early stage of hit identification to assess the spatial proximity of the warhead to the target cysteine.

Scan of Protein Target Site and Assessment of Proximity. The β-methyl-substituted enone (2) and its corresponding moderately electrophilic derivative, β,β-dimethyl enone (3), were selected to explore the target space. A collection of compounds with pairwise matched linkers but either fast (2, 10−12) or moderately (3, 13−15a) reactive Michael acceptors were synthesized (Figure 3a).

When bound to the adenosine 5′-triphosphate (ATP)-binding site of PI3Kα, the linker length of the covalent inhibitor defines the proximity of the warhead to Cys862. As explained below in detail, the warhead will thus reside within a reactive volume (V_r), which defines the local concentration of the sulfhydryl group of Cys862 and the β-carbon of the Michael acceptor of the warhead. Based on molecular modeling, V_r can be approximated by a sphere with a radius equal to the distance of the warhead and Cys862 (Figure 3b and Table S4). An excellent correlation was obtained between the predicted local concentration (estimated by $1/(N_A·V_r)$; N_A, Avogadro's number) of the warhead and the rate constant for the irreversible reaction with Cys862 (k_{inact}; $R^2 = 0.999$, Figure 3c). The irreversible reaction rate k_{inact} was determined using a time-resolved fluorescence resonance energy transfer (TR-FRET) tracer displacement assay. Fitting time- and concentration-dependent TR-FRET ratio curves (Figure S2) using KinTek kinetic modeling software yielded k_{inact}, the calculated K_i, and a k_{inact}/K_i ratio typically used to characterize the covalent binding
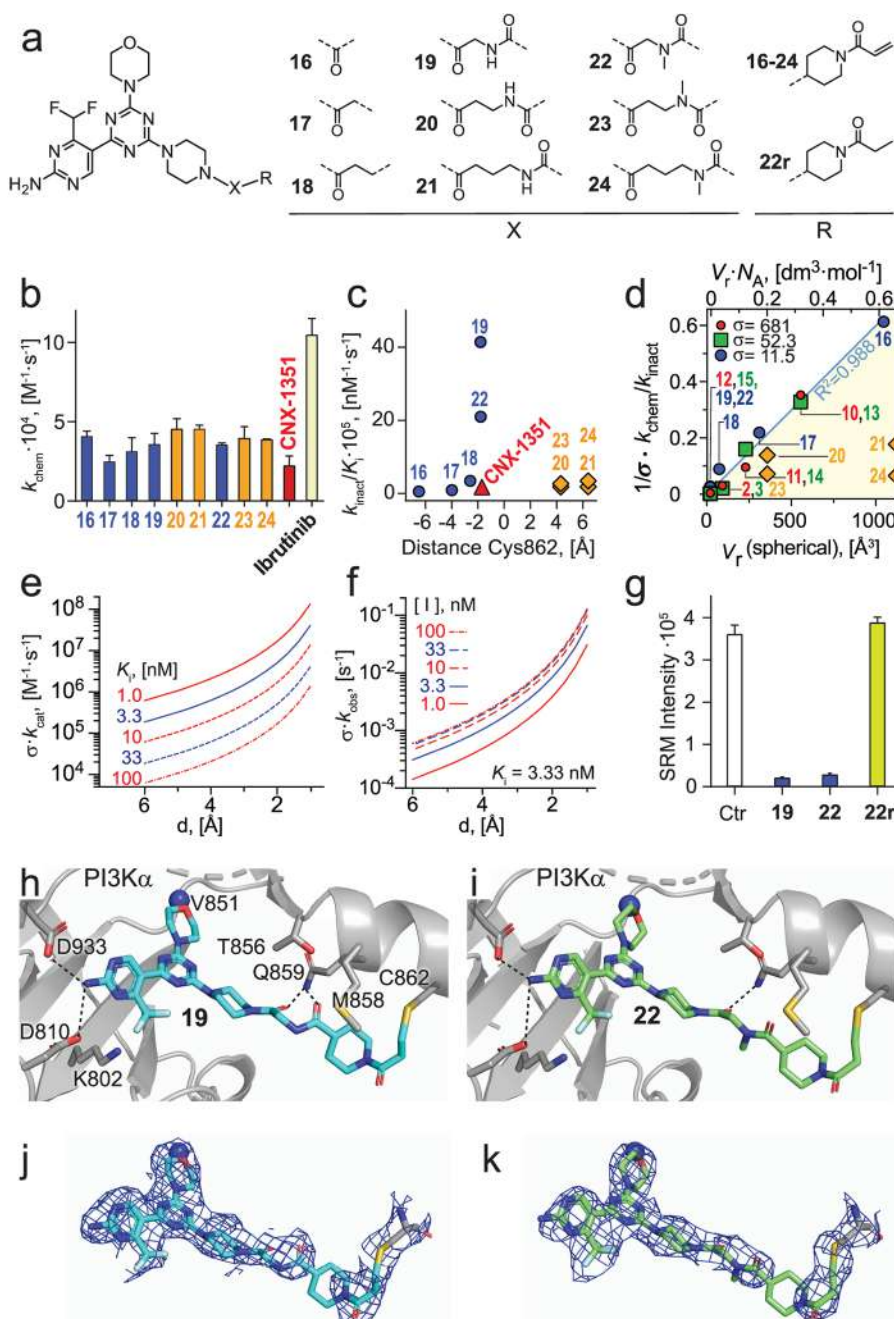
Figure 4. (a) Library of acrylamide-containing compounds (**16−24**). (b) Intrinsic reactivity (k_{chem}) of compounds **16−24**, ibrutinib and CNX-1351. Experiments performed with HPLC (1 mM inhibitor and 600 mM βME, n = 3). All values are reported as mean ± SD. Error bars are not shown when smaller than the symbols. (c) Efficiency in covalent bond formation (k_{inact}/K_i) plotted against distance from Cys862. Zero on the x-axis corresponds to Cys862 positioning; zero to left: shorter linkers; zero to right: longer linkers. Kinetic parameters are reported in Table S5. The distances between the Michael acceptors (β-carbons) and Cys862 thiol were calculated using Maestro 11.1 and PyMOL 2.3.5 Schrödinger LLC (see Figure S5). (d) Plot of k_{chem}/k_{inact} ratios vs the reactive volume V_r of compounds **12, 2, 11, 10** (red circles), **15a, 3, 14, 13** (green squares), **19, 22, 18, 17, 16** (blue circles), and **20, 23, 21, 24** (orange diamonds). The top x-axis shows the $V_r \cdot N_A$ term utilized as in eq S14b to determine the scaling factor σ for each compound group as shown in Figure S7 and Table S6. The compound group-specific σ factors were used to normalize the k_{chem}/k_{inact} ratios by $1/\sigma$. The (blue) regression line includes all compounds listed above except for **20, 23, 21, 24**, with a linker reaching beyond the target Cys862. (e) Normalized k_{cat} reaction rates were calculated according to eq 15 with a spherical V_r approximation using the modeled distance to the target d. For K_i, the indicated values were used. (f) Normalized k_{cat} reaction rates were calculated according to eq 17a as a function of d and the inhibitor concentration [I]. For both graphs in (e) and (f), a mean k_{chem} averaged over the values from compounds **19, 22, 18, 17,** and **16** was used ($k_{chem\,(19, 22, 18, 17, 16)}$ = 3.38 × 10^{-4} M^{-1}· s^{-1}). (g) LC-SRM quantification of Cys862-modification by **19, 22,** and **22r**. (h, i) X-ray structure of (h) **19** (deep teal) bound to PI3Kα (PDB ID 7R9V, resolution 2.69 Å) and (i) **22** (deep purple) bound to PI3Kα (PDB ID 7R9Y, resolution 2.85 Å). H-bonds are depicted as dashed black lines. As for the CHF$_2$-group, a H-bond either with (i) Lys802 or with (ii) the triazine core (intramolecular interaction) is possible based on the proton positioning. (j, k) Electron density maps of the inhibitor (2Fo−Fc map contoured at 1σ, blue mesh) fit the structure of (j) **19** and (k) **22**, and the electron density clearly shows that the acrylamide forms a covalent bond with the thiol group of Cys862.

Table 1. Key Parameters for Acrylamide Derivatives (16−24), CNX-1351, Ibrutinib

compound	$k_{chem} \times 10^4$ (M^{-1}·s^{-1})	k_{inact} PI3K$\alpha \times 10^4$ (s^{-1})[a]	K_i PI3Kα (nM)[a]	$k_{inact}/K_i \times 10^5$ (nM^{-1}·s^{-1})[a]	IC$_{50}$ pPKB (S473) SKOV3[c]
16	4.10	0.58	10.8	0.54	51
17	2.49	0.98	10.7	0.93	47
18	3.07	2.92	8.56	3.43	48
19	3.70	12.0	2.93	41.4	82
20	4.52	2.52	14.0	1.80	664
21	4.37	1.95	10.6	1.87	686
22	3.54	10.8	5.14	21.0	86
23	3.88	3.78	14.5	2.61	250
24	3.86	4.06	12.2	3.36	260
19r		0[b]	2.55	0[b]	200
22r		0[b]	6.15	0[b]	227
CNX-1351	2.22	6.57	38.0	1.74	165
ibrutinib	10.4				

[a]Mean (and SD) were calculated from three independent measurements. [b]Values modeled with KinTek Global Kinetic Explorer are lower than 10^{-11} (nM^{-1}·s^{-1}), no covalent reaction was detected. The full dataset and SD are reported in Table S5. [c]Mean (and SD) were calculated from three independent measurements.

of irreversible inhibitors to the target protein (Table S3). The time- and concentration-dependent TR-FRET data can be represented as time-dependent IC$_{50}$ curves (exposure times of 10, 15, 30, 60, and 90 min), where a shift in IC$_{50}$ visualizes a covalent, time-dependent reaction of inhibitors with PI3Kα (Figure 3d,e). For compounds bearing a fast-reacting warhead (**2, 10−12**) a significant IC$_{50}$ shift was observed even when their Michael acceptor was predicted to be located at >3.5 Å from Cys862 thiol (**10**: 5.1 Å and **11**: 3.8 Å; Figures 3d and S3). Compounds **2** and **12**, with longer linear linkers (n = 3 and 4), displayed an increased efficiency in covalent bond formation with PI3Kα, and compound **12** showed the highest rate of covalent inactivation ($k_{inact}/K_i = 1.27 \times 10^{-3}$ nM^{-1}·s^{-1}, Table S3). Reversible analogues did not display a time-dependent IC$_{50}$ shift (Figure 3j for **2r**). Similarly, β,β-dimethyl enone-containing compounds **13** and **14** showed no detectable IC$_{50}$ shift (Figure 3e) and very low k_{inact}/K_i ratios (**13**: 3.25×10^{-6} and **14**: 3.21×10^{-6} nM^{-1}·s^{-1}) compatible with negligible covalent target engagement. Compound **15a**, placing the warhead <2 Å from Cys862, showed an increased k_{inact}/K_i ratio (5.82×10^{-5} nM^{-1}·s^{-1}, Table S3). The fact that **15a** displayed a 22-fold lower k_{inact}/K_i ratio compared to **12** with an identical linker length demonstrates that the faster warhead in **12** is much better suited to monitor the proximity to the target.

The increase in linker length did not influence the intrinsic reactivity of the inhibitors for both fast and moderately reactive Michael acceptors (Figure 3f). The reversible binding (see K_i, Figure 3g) was moderately attenuated by extended hydrophobic linkers in a solvent-exposed region of the ATP-binding site. These two findings clearly illustrate that the increased efficiency in covalent bond formation for **12** is related to the optimized proximity of the warhead to Cys862. The comparison of molecules with equal linker length and fast vs moderate reactivity warheads shows clearly that fast warheads produce a significant increase in k_{inact} (Figure 3h) and k_{inact}/K_i (Figure 3i) producing a proximity "hit alert" that is not detected with moderately reactive compounds. Fast-reactive warheads therefore provide an exquisite opportunity to rapidly (i) approach a nucleophilic target in biologically relevant proteins and (ii) prove the feasibility to convert a reversible scaffold into a covalent molecule.

To complement the experimental approaches, modeling of covalent docking was performed using CovDock Schrö-

dinger.[57,58] As CovDock affinity values are only reliable when intrinsic warhead reactivities are equal,[57] they cannot be exploited to compare our different hit sets including compounds with enones and acrylamides (**2, 3**, and **10−24**). Therefore, as an output parameter, we assessed the displacement of the PI3K-binding core module from the hinge (V851) and the binding affinity region (D810) after covalent binding to Cys862. Fifty poses per ligand were generated, and the distance between (i) the morpholine oxygen atom (O17) and the backbone amide nitrogen atom of Val851 (O17-V851, Figure 3a,k), and (ii) the amino group (N26) of the aminopyrimidine and the closest oxygen in the side chain carboxylate of Asp810 (N26-D810, Figure 3a,k) were calculated. Considering the compounds **2** and **10−12**, the morpholine oxygen (O17) of **12** was juxtaposed with that of PQR530 (PDB ID 6OAC)[59] (Figure 3k), highlighting that the reversible core module was well accommodated in the ATP-site upon the modeling of the covalent reaction with Cys862. On the contrary, the morpholine oxygen in compound **10** was displaced by ∼2 Å (Figure 3k) to allow the warhead to react with Cys862. A similar trend was observed determining the N26-D810 distance, where N26 of compounds **10** and **11** was displaced by ∼1.8 and 2.5 Å, respectively, compared to N26 in **12** (Figure 3l). Analysis of the whole panel of compounds, shown in Figure S6, pointed out that CovDock can be exploited to narrow down the hit list in covalent inhibitor design, and allows the exclusion of molecules with a bad match in linker length.

A further demonstration that the scan of the target site is more likely to succeed using reactive warheads was demonstrated with acrylamide compounds **15b** and **15c**, which showed a drop of k_{inact} to 0.96×10^{-4} and 1.27×10^{-4} s^{-1}, respectively, compared to a k_{inact} of 9.03×10^{-4} s^{-1} for **15a**.

Linker Optimization Using Druglike Warheads. As shown above, unsubstituted acrylamides (**4** and **7**) can be exploited in covalent chemical probes with minimal off-target reactions with unspecific nucleophiles inside cells (Figure 2i). To correlate the spatial trajectory to Cys862 with the above warhead series (see Figure S14), nine molecules (**16−24**, Figure 4a) bearing an acrylamide warhead and different linker modules were synthesized. A piperidine ring was introduced in these molecules as the attachment point for the warhead. Piperidine has been proposed as a privileged scaffold in drug discovery and is present in many marketed anticancer agents.[60] The piperidine

ring was connected to the PI3Kα-binding module through a carbon-chain (**16–18**) or an amide-containing (**19–24**) linker. Two possibilities have been explored for amide-linker compounds: secondary (compounds **19–21**) and tertiary (**22–24**) amides were introduced (Figure 4a). The presence of an additional methyl slightly affected the physicochemical properties (clog P, see Table S5) and inhibitor–protein affinity (see next section).

Intrinsic reaction rates (k_{chem}) were measured by adduct formation with βME, to validate that chemical modifications of the linker did not affect the electrophilicity of the acrylamide warhead. All compounds displayed similar intrinsic reactivities, matching the values of CNX-1351 and ibrutinib (see the Supporting Information for chemical structures) within the same order of magnitude (Figure 4b). TR-FRET measurements of k_{inact}, K_i, and calculation of k_{inact}/K_i, as reported in Table S5, document that the efficiency of covalent bond formation was dramatically increased passing from compound **16** to **19** and **22** (see Figure S4 for time- and concentration-dependent TR-FRET ratio curves used for parameter fitting, and Figure S5 for distance measurements). After reaching a maximum efficiency in covalent bond formation (**19** and **22** k_{inact}/K_i = 4.14 × 10^{-4} and 2.10 × 10^{-4} nM^{-1}·s^{-1}, respectively; Table 1), a drop in k_{inact}/K_i values was observed further elongating the linker beyond Cys862 (compounds **20**, **21**, **23** and **24**, Figure 4c). Our data show that the excellent reactivity of **19** and **22** with PI3Kα is related to the optimal positioning of the warhead close to Cys862 and is not influenced by intrinsic warhead reactivity (Figure 4b,c). Compounds **19** and **22** displayed k_{inact}/K_i values >10–20 times higher than that of CNX-1351 (41.4, 21.0 vs 1.74 × 10^{-5} M^{-1}·s^{-1}).

Stochastic Approach to Calculation of Covalent Reaction Rates as $f(k_{chem}, k_{inact}, K_i,$ and $V_r)$. To better understand how the various kinetic parameters influence the overall covalent reaction rates, we developed a novel stochastic approach to describe the relation of k_{chem}, k_{inact}, K_i, and the distance of the warhead to the target cysteine (d), which defines the reactive volume V_r. Our proposed model unites the macroscopic and microscopic parameters of the covalent reaction and takes into account the probabilistic nature of the chemical reactions. Using Chemical Master Equations (CME), we derived a linear relation of the k_{chem}/k_{inact} ratio to the reactive volume V_r (eq 14a), for all equations and their full derivation, see the Supporting Information, SI.

$$k_{inact} \cdot \sigma = \frac{k_{chem}}{N_A \cdot V_r} \tag{14a}$$

Here, σ is a scaling factor, which allows for the compensation for nonintrinsic warhead reactivity due to the steric effects and the warhead's chemical environment. The application of the model to three groups of covalent PI3Kα inhibitors (**2** and **10–12**; **3** and **13–15a**; **16–19** and **22**) showed that k_{chem}/k_{inact} ratios plotted vs V_r fit a simple linear relationship (R^2 = 0.98, 0.98 and 0.99, respectively; see Figure S7 and Table S6), and thus validate the proposed eq S14b.

Moreover, the scaling factor allows the association of the three investigated compound groups in unified k_{chem}/k_{inact} ratio to reactive volume V_r plots as depicted in Figure 4d. The excellent linear fit obtained in Figure 4d (R^2 for **2**, **10–12**, **3**, **13–15a**; **16–19**, and **22** was 0.988) characterizes σ as a useful predictor of changing compound properties, but also visualizes deviations in the targeting approach: compounds **20**, **21**, **23**, and **24**, with

linker reaching beyond the targeted Cys862, appear below the regression line when fitted using the σ derived from compounds **16–19** and **22** based on the similarity of warhead structure and environment. This illustrates that the k_{inact} values of **20**, **21**, **23**, and **24** are larger than predicted based on the spherical approximation of V_r. The reason for this is that molecules with linkers reaching beyond the target Cys can bend and fold back to form Cys adducts while still bound to the ATP-binding site. Molecules with a short linker must detach from the ATP-binding site to reach the target Cys (Figure 3k,l).

Also, the resulting interactions between warhead and target cysteine may be altered by the steric constraints. Overall, the results indicate that molecules with longer linkers have an increased probability to bind to Cys862 as predicted from a distance from the warhead to the Cys when measured in a stretched conformation, which in turn yields higher k_{inact} values and consequently lower k_{chem}/k_{inact} ratios. This shows some limitations of the current V_r estimation when outside of the validated distance from the target Cys (see Figure 4d). Future improvements and inclusion of steric factor calculations in the $\sigma \cdot V_r$ term will extend its validity across diverse structurally restricted linkers.

The stochastic approach also allows the integration of equations established by Copeland[61] and Strelow[62] to calculate k_{cat} and k_{obs} values and to predict overall rates as a function of k_{chem}, k_{inact}, K_i, and V_r

$$\frac{k_{inact}}{K_i} = k_{cat} = \frac{1}{\sigma} \cdot \frac{k_{chem}}{K_i \cdot N_A \cdot V_r} \tag{15}$$

$$k_{obs} = \frac{1}{\sigma} \cdot \frac{k_{chem}}{N_A \cdot V_r} \cdot \frac{1}{(1 + K_i/[I])} \tag{17a}$$

These equations can be utilized to generally define the dependencies of reaction rates as a function of K_i and the inhibitor concentration, [I]: as shown in Figure 4e for the dependency of k_{cat} on the distance to target Cys (d) and K_i, the reversible affinity to the target (K_i) is important, but an improvement in K_i by a factor of ~10 can be matched by a closer approach to the Cys by ca. 3Å. This illustrates that the distance of the warhead to the target cysteine dominates k_{cat}. For k_{obs}, the overall rate of the covalent reaction, values converge rapidly to a maximal value if [I] > K_i, but can still be dramatically accelerated by shortening the distance to the targeted nucleophile (Figure 4f).

Confirmation of Covalent Cys862 Engagement. The covalent bonds between compounds **19** and **22** and the targeted Cys862 in PI3Kα were confirmed by mass spectrometry and X-ray crystallography. Bottom-up LC-MS/MS-based proteomics demonstrated covalent modification of Cys862 by compounds **19** and **22**. A reversible analogue of compound **22** (**22r**) was synthesized (Scheme S3) and used as a negative control. A selective covalent modification of Cys862-containing tryptic peptide (NSHTIMQIQCK) was observed for **19** and **22**, but not for **22r**. MS1 extracted-ion chromatogram (XIC) traces are reported in Figure S8. Afterward, the presence of modified forms of NSHTIMQIQCK was established by peptide-spectrum matching. All MS2 spectra were searched against the whole set of human entries of the Uniprot database (20 308 total protein entries). Only peptide spectrum matches with a high confidence (>0.9) were considered (see proteomics data in the Supporting Information). Among these, the only compound-modified peptide was NSHTIMQIQCK carrying **19** and **22** (Table S7).
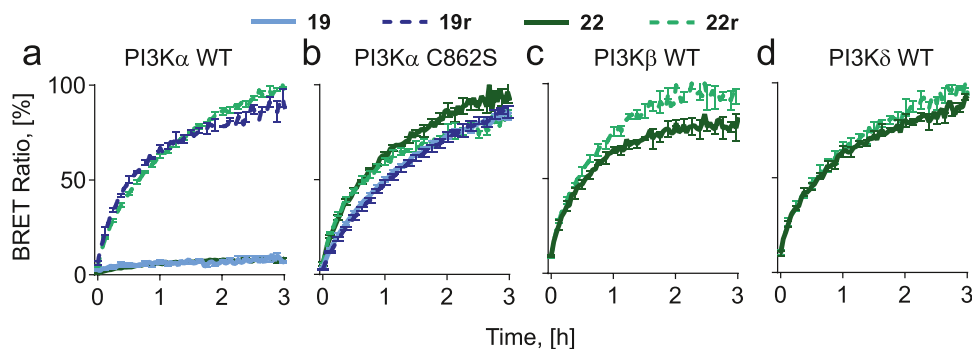
Figure 5. (a−d) Residence time experiment using BRET in intact HEK293 cells expressing NanoLuc fused to (a) PI3Kα, (b) PI3Kα Cys862Ser, (c) PI3Kβ, and (d) PI3Kδ. The cells were incubated with inhibitors (3 μM) for 2 h. Subsequently, free inhibitor was washed out twice using Opti-MEM medium (for 10 min at 37 °C and 5% CO_2), before the cell-permeable BRET tracer was added (0.2 μM final concentration). A tracer bearing a pyrrolylBODIPY fluorescent moiety[83] (excitation at 460 nm and emission at 618 nm) was used to determine the on-target residence time of the inhibitors after drug washout.[64] Displacement of the inhibitors by the BRET tracer from the ATP-binding pocket in the indicated PI3K isoforms was monitored by the recovery of the BRET signal between the NanoLuc-fused PI3K (donor) and the BRET tracer (acceptor). A prolonged residence time of inhibitors (after drug washout) diminishes the BRET signal and points to a covalent interaction. Data shown are mean ± standard error of the mean (SEM) (n = 3). Results for CNX-1351 are shown in Figure S10.

The fragment spectra were assigned with a very high confidence of >99.9% (Figure S9). LC-SRM was used to quantify the conversion rates of Cys862 by **19**, **22**, and **22r**. The reactive compounds displayed a conversion rate >90% (**19**: 94% and **22**: 92%), while no conversion was observed for the reversible analogue **22r** (Figure 4g).

X-ray crystallographic studies with compounds **19** and **22** mapped continuous electron densities between the side-chain thiol group of Cys862 and the inhibitors' acrylamide moiety, indicating the formation of a covalent bond between PI3Kα and the inhibitor (Figure 4h,i). Due to linker flexibility, a gap in the electron density map was observed for both **19** and **22** (Figure 4j,k). The core molecule maintained the major interactions observed for the PI3Kα-PQR530 complex (PDB ID: 6OAC, resolution 3.15 Å),[59] including the H-bond between the morpholine oxygen and the backbone amide of Val851, as well as between the NH_2-group of the aminopyrimidine and Asp805/810. The CHF_2-group could either interact (i) with the triazine core in an intramolecular manner or (ii) with Lys802 (distances <2.5 Å). The linker connecting the core module with the warhead is located in the solvent-exposed region and the carbonyl group linked to the piperazine establishes a pivotal interaction with Gln859 (distance <3.0 Å) for both **19** and **22** structures (Figure 4h,i). Met858 and Thr856 interact differently with **19** and **22** linkers due to the higher rigidity of the tertiary amide, leading to an optimal stabilization of **19** (see Figure 4c for k_{inact}/K_i values). Altogether these results confirm that **19** and **22** irreversibly inhibit PI3Kα by a covalent modification of Cys862.

NanoBRET Assay Detects Drug-Target Engagement in Cells. A bioluminescence resonance energy transfer (BRET) inhibitor displacement assay was used to dynamically quantify target engagement in living cells. The used NanoBRET approach exploits light emission from a small, bright, and stable Nanoluciferase (NanoLuc)[63,64] fused to PI3Ks, and an energy transfer to a fluorescent (a pyrrolylBODIPY tracer; Energy Transfer Probe 3 in ref 62) tracer binding to the ATP-binding pocket of PI3Ks. We have examined the irreversible covalent behavior of **19** and **22** in HEK293 cells expressing NanoLuc-PI3K fusion proteins (PI3Kα, a PI3Kα Cys862 to Ser mutant, PI3Kβ, and PI3Kδ). The reversible analogues of **19** and **22** (**19r** and **22r**) were included as negative controls (Figure 5), and

CNX-1351 as a positive control (Figure S10). After exposure to **19** or **22**, subsequent inhibitor washout, and tracer addition, the cells expressing wild-type PI3Kα did not show a BRET signal and tracer binding for >3 h (Figure 5a). In contrast, the PI3Kα C862S mutant displayed comparable dissociation rates for **19**, **22**, and their corresponding reversible analogues **19r** and **22r** (Figure 5b). Tracer binding and BRET signal increase were achieved also after drug washout in PI3Kβ and PI3Kδ (Figure 5c,d). The NanoBRET assays demonstrated therefore that compounds **19** and **22** selectively and irreversibly react with Cys862 in wild-type PI3Kα, but not with PI3Kα C862S, PI3Kβ, and PI3Kδ.

Validation of Extended Duration of Action in Cellular Washout Studies. The library of acrylamide-containing compounds (**16−24**) was evaluated in SKOV3 ovarian cancer cells with a constitutively active PI3Kα due to a His1047 to Arg mutation in *PIK3CA*[65] and enhanced expression of ERBB2 (HER2).[66] PI3K output was monitored by protein kinase B (PKB/Akt) phosphorylation on Ser473. Compounds **19** and **22** displayed a good cellular activity (IC_{50} for PKB/Akt phosphorylation was 82 and 86 nM, respectively), being twice as potent in SKOV3 cells compared to CNX-1351 (IC_{50} of 165 nM, Tables 1 and S5). Despite the poor efficiency in covalent bond formation, compounds **16−18** showed high cellular potency (IC_{50} of 51, 47, 48 nM, Table 1) due to the increased clog P compared to **19** and **22** (clog P: **16**: 1.72; **17**: 1.89; **18**: 2.28; **19**: 0.65; **22**: 0.89, Table S5).

To gain further insight into long-term inhibition of PI3K signaling, cell lines with mutated, constitutively activated PI3Kα (MCF7 breast carcinoma, *PIK3CA* Glu545Lys; SKOV3 ovarian carcinoma, His1047Arg; and T47D breast carcinoma, His1047Arg)[65] were exposed to compounds **19**, **22**, and their reversible analogues (**19r** and **22r**) lacking the Michael acceptor (see Scheme S3), as well as BYL719. BYL719[35] was used as a reversible inhibitor benchmark. The cells were incubated with inhibitor (3 μM for 2 h) before free compound was washed out. Subsequently, PI3K signaling output was measured by in-cell western (ICW) detection of phosphorylated PKB/Akt. A complete and prolonged inhibition (>6 h) of PKB/Akt phosphorylation was observed in MCF7 (Figure 6a,b) and T47D (Figure 6c,d) cells after washout of **19** and **22**, demonstrating that the irreversible elimination of PI3Kα activity
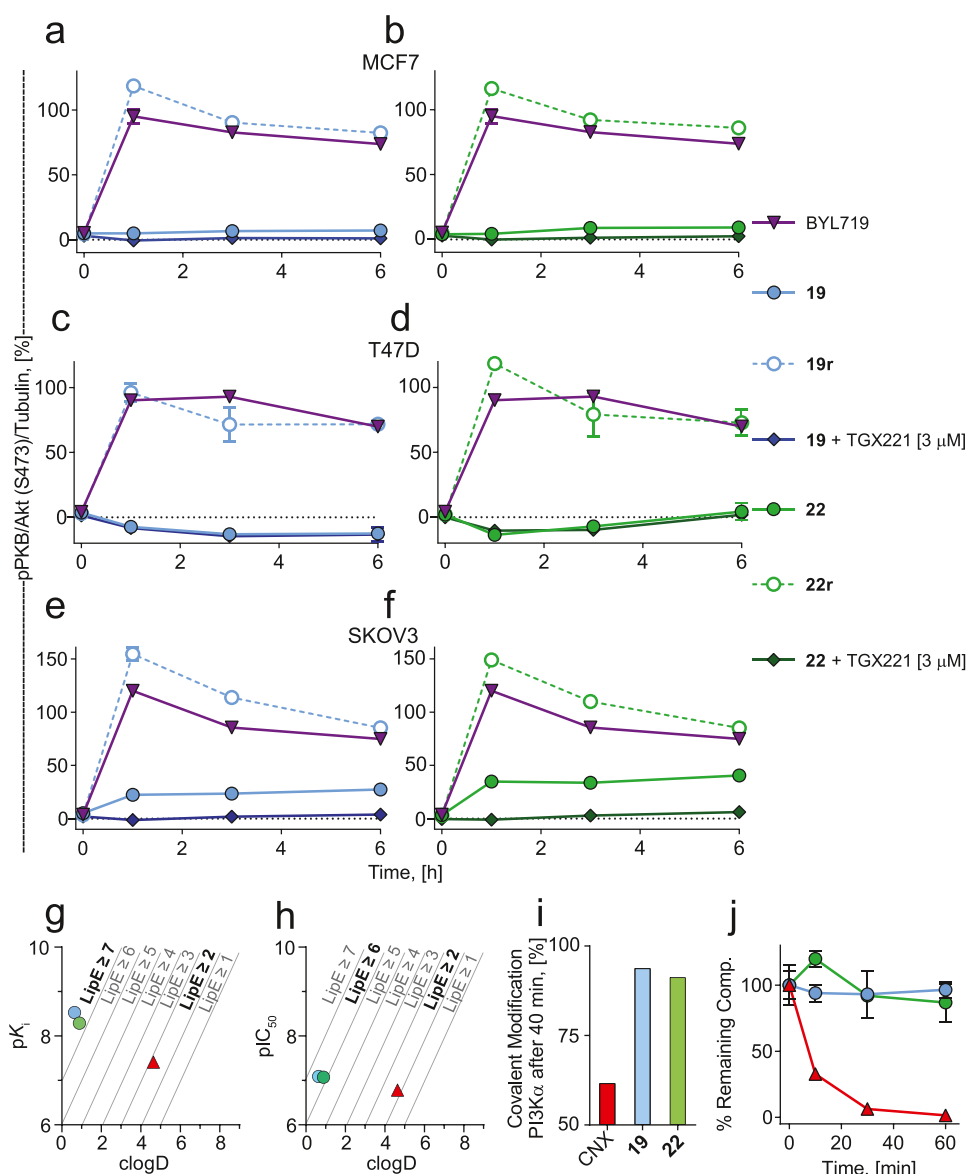
Figure 6. (a−f) Cellular washout experiments in cancer cells with a mutated and constitutively activated PI3Kα. (a, b) MCF7 (*PIK3CA* E545K), (c, d) T47D (*PIK3CA* H1047R), and (e, f) SKOV3 (*PIK3CA* H1047R; *HER2*+) cancer cell lines were treated with 3 μM of the indicated compounds for 2 h, followed by drug washout (twice with fully supplemented Dulbecco's modified Eagle's medium (DMEM) for 10 min each). The cells were then incubated at 37 °C and 5% CO_2 for the indicated times before they were fixed, and the phosphorylation status of PKB/Akt was determined by in-cell western; $t = 0$ values indicate reference measurements in the presence of inhibitor (i.e., immediately after the 2 h treatment window and without removal of drug). Where indicated, TGX221 (3 μM) was added 1 h before the fixation of cells, to investigate a potential cell-line-dependent further contribution of PI3Kβ to PKB/Akt phosphorylation. Data shown are mean ± SEM ($n = 4$; two independent measurements). Error bars are not shown when smaller than symbols. (g, h) Plot of clog *D* vs biological activity ((g) pK_i; (h) pIC_{50}) of compounds **19**, **22**, and CNX-1351. Lipophilic ligand efficiency (LipE) values higher than 5 are considered to be the threshold for lead compounds and high-quality chemical probes. LipE calculations are shown in Table S9. (i) On-target covalent modification modeled after 40 min using KinTek Global Kinetic Explorer. See Figure S1c,d for additional details. (j) Metabolic stability of **19**, **22**, and CNX-1351 using rat liver microsomes fortified with phase I metabolism cofactor NADPH. The time-dependent degradation of test items (starting concentration 1 μM) in the presence of rat liver microsomes (0.5 mg microsomal protein/mL) was measured (mean ± SD; $n = 2$). Error bars are not shown when smaller than symbols. Corresponding raw data are reported in Table S10.

was sufficient to fully downregulate all PI3K signaling. This suggests that mutated PI3Kα is the prevalent driver of PI3K signaling in these cells. In contrast, ca. 25% of PKB/Akt phosphorylation persisted in SKOV3 cells after the washout of **19** or **22** (Figure 6e,f), which is best explained by the enforced signaling of over-expressed HER2 to other class IA PI3K. In line with this, further addition of the PI3Kβ-selective inhibitor TGX221[67] after the transient exposure to either **19** or **22** yielded

a complete inhibition of PI3K signaling also in SKOV3 cells (Figure 6e,f).

In the presence of all inhibitors (before washout, $t = 0$), including the reversible **19r**, **22r**, and BYL719, PI3K output was completely blocked. This illustrates that BYL719 also inhibited the TGX221-sensitive PI3Kβ signaling in SKOV3 cells and acted as pan-PI3Ki. Altogether, an incubation/washout cycle with **19** and **22** reveals reliably which part of a PI3K output is

strictly PI3Kα-dependent, and qualifies **19** and **22** as specific chemical probes to investigate selectively PI3Kα signaling.

Lipophilicity and Lipophilic Ligand Efficiency (LipE). Lipophilicity plays a central role in compounds' pharmacokinetics and safety; thus, the concept of lipophilic ligand efficiency (LipE) has been developed to normalize potency relative to lipophilicity. The potential of achieving good in vivo performance increases when chemical modifications improved potency and simultaneously lower lipophilicity.[68] Proposed acceptable values of LipE for drug candidates are ≥5.[69] We calculated LipE values for our lead compounds (**19** and **22**) as well as CNX-1351 to evaluate the effect of the structural changes on both potency and lipophilicity. LipE profiles of CNX-1351 did not reach the standard threshold value of 5 [LipE (K_i) = 2.78; (IC_{50}) = 2.13, Figure 6g,h; see Table S9 for calculations]. On the contrary, compounds **19** and **22** significantly increased potency and decreased lipophilicity, resulting in optimal LipE values [LipE (K_i) = **19**, 7.89; **22**, 7.40; LipE (IC_{50}) = **19**, 6.44; **22**, 6.18, Figure 6g,h]. Employing LipE allowed to move into the desirable property space and to select high-quality chemical probes. Based on KinTek modeling using experimentally determined K_i and k_{inact}, **19** and **22** predicted to reach covalent modification of PI3Kα faster than with CNX-1351 (Figure 6i). KinTek modeling also predicts that all three compounds display negligible off-target reactivity (Figure S1d).

Assessment of Metabolic Stability. The metabolic stability of **19**, **22**, and CNX-1351 was evaluated in vitro in rat liver microsomes fortified with NADPH as a phase I metabolism cofactor. Compounds were tested at 1 μM concentration with liver microsomes and the percentage of remaining compounds after 60 min of incubation was detected. Verapamil was run in parallel as a high-clearance control compound. Compounds **19** and **22** were stable over the tested time frame with 97% of **19** and 87% of **22** remaining. CNX-1351 was rapidly metabolized with only 2% remaining after 60 min of incubation (Figure 6j and Table S10). Compounds **19** and **22**, containing a moderately reactive, druglike warhead, as well as a metabolically favorable linker, outperformed the rapidly metabolized CNX-1351.

Profiling of Protein and Lipid Kinase Selectivity. Although off-target reactions with free thiols are negligible for **19** due to its low inherent reactivity, reversible binding to off-target proteins could generate the proximity to bring about off-target reactions. As **19** contains an ATP-site binding module, protein kinases are a possible target. The cysteinome of protein kinases has been elegantly reviewed by Chaikuad et al.[70] and provides a projection of the cysteinome to protein kinase A (PKA). Modeling of **19** into this template's ATP-binding reveals only one close target cysteine at a distance of ca. 8 Å, which belongs to the c-Jun amino-terminal kinase (JNK1, 2, 3) family (Figure 7a, Cys154 in JNK3, labeled as F3) and previously targeted by the selective, covalent JNK-IN-8 inhibitor.[71]

To explore the selectivity of compound **19** for PI3K, a DiscoverX scanMAX kinase assay panel including a wide range of protein and lipid kinases was used. Compound **19** displayed negligible binding to protein kinases including JNK1-3 at a concentration of 1 μM (Figure 7b, full dataset and comparisons with PQR514, PQR309, BYL719, GDC-0980, and PKI-587 in Figure S11 and Table S13). The only minor hits involved CSF1R (autoinhibited), JAK1 (JH2 domain-pseudokinase), KIT (autoinhibited), with a remaining tracer binding of 20, 32, and 35%, respectively. At the same time, CSF1R, JAK1, and KIT (and mutant) catalytic domains showed no relevant interactions
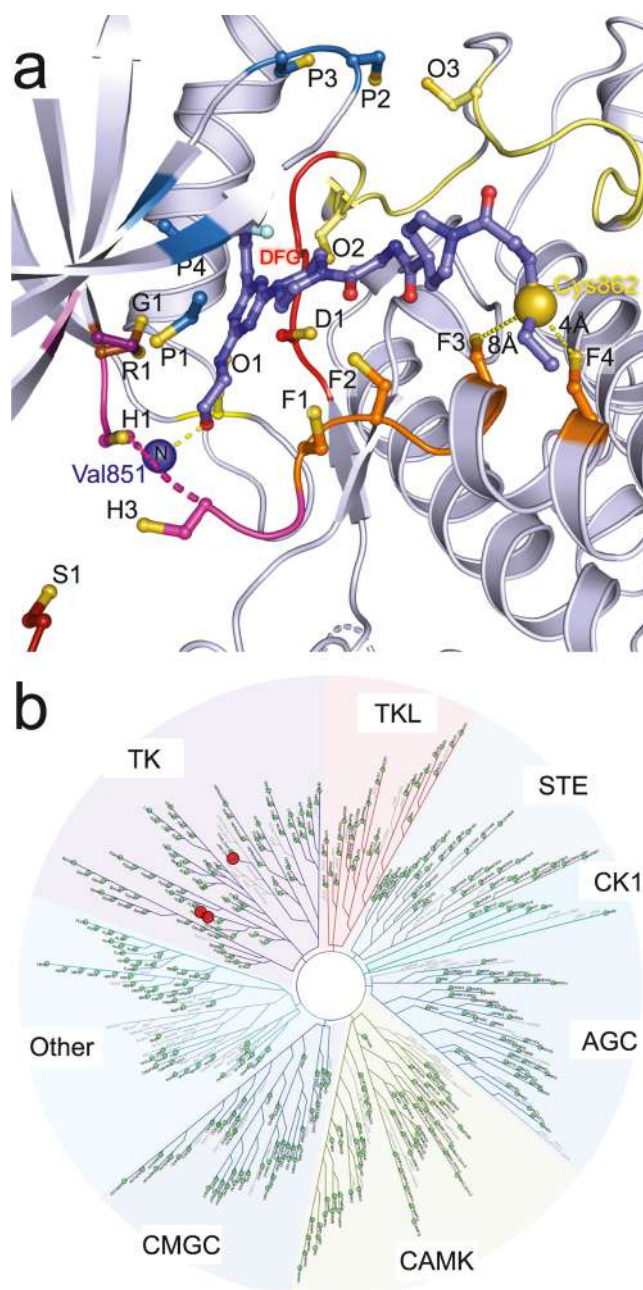

Figure 7. (a) Analysis of putative off-target reactions of covalent PI3Kα inhibitors with protein kinases. Coordinates for a cysteinome protein kinase template were kindly provided by Chaikuad and Knapp. Their template was generated based on the PDB ID 1ATP of the catalytic subunit of cAMP-dependent protein kinase (PKA), onto which cysteines throughout the kinome have been projected as reported in ref 70. These coordinates were aligned with PI3K crystallographic data from PDB IDs 5OQ4 (PQR309/PI3Kγ complex), 1E8X (ATP/PI3Kγ complex), and structures of compound **19** bound to PI3Kα provided here, to dock **19** into the PKA template's ATP-binding site. In the depicted compound **19** (dark blue), the sulfur atom of Cys862 (oversize yellow sphere) is located at a distance of 8.0 Å from Cys F3 (Cys annotation as in ref 70), which corresponds to a Cys in JNK1, 2, and 3. Closer is only Cys F4 at a distance of 4.0 Å, which is the Cys862 of PI3Kα projected onto the PKA template. The rest of the projected protein kinase Cys residues are ≫10 Å away from the warhead of **19** and cannot be targeted without displacement of the ATP-binding module. (b) Validation of off-target binding of **19** at 1 μM to protein kinases in KINOMEScan experiments (comparisons with results from PQR514, PQR309, BYL719, GDC-0980, and PKI-587, and lipid kinase

Figure 7. continued

interactions are shown in Figure S11 and quantitative data are listed in Table S13). The three red spots in the kinase tree represent CSF1R (autoinhibited; juxtamembrane domains of some protein tyrosine kinase receptors stabilize the kinase domain in an inactive state), JAK1 (JH2 domain-pseudokinase), and KIT (autoinhibited) with remaining binding of 20, 32, and 35%, respectively. CSF1R, JAK1, and KIT (and mutant) catalytic domains (in active conformations) showed no relevant interactions with **19**.

---

with **19**, as also apparent from excellent selectivity scores (Table S12). This selectivity is based in part on the PI3K-binding motif derived from PQR514, a compound that shows a K_d of 2 nM for PI3Kα in a KdELECT assay (Table S11), which drops to 0.1 nM by a factor of 20 for **19**.

Compound **19** is thus a potent covalent PI3Kα inhibitor and acts at higher concentrations as pan-PI3K. This profile allows the transient, reversible inhibition of class I PI3Ks (PI3Kβ, PI3Kδ, and PI3Kγ; Table S11), while PI3Kα inactivation persists after the washout of free inhibitor and completely abrogates PI3K signaling in cells with mutated, constitutively activated PI3Kα (Figure 6).

Our novel covalent tools have been fully characterized and met all of the criteria proposed in the validation process of a covalent tool compound,[72] including (i) irreversible ligand and control compounds; (ii) time-dependent in vitro activity; (iii) retained cell-based activity upon washout; (iv) confirmed target labeling using mass spectrometry; (v) confirmed residue-specific labeling using X-ray crystallography and/or MS; (vi) cell-based target validation (resistance mutation, C862S); and (vii) selectivity profiling (KinomeScan, TreeSpot representation).

CONCLUSIONS

Selective irreversible inhibition relies on warhead reactivity and proximity. Here, we delineate a path to an efficient design to proximity-optimized druglike covalent inhibitors targeting remote cysteines. As moderate electrophiles with a distant target nucleophile do not produce hits in assays for covalency, we use fast-reactive warheads as tools in an early stage of the screening process to explore a bigger reactive space. The proximity/reactivity (k_{inact}) information acquired as a function of linker length served then to design molecules with an expected placement of the warhead in close proximity to the target cysteine. At that stage, acrylamide-containing warheads could be introduced, avoiding metabolic instability and off-target thiol reactivity. The optimization of linkers allowed a close positioning of the electrophile relative to Cys862 in PI3Kα. A thorough assessment of intrinsic chemical reactivity (k_{chem}) and rate of covalent bond formation (k_{inact}) with PI3Kα provided a guided path to proximity-driven reactivity. Following this recipe, a two-order of magnitude increase in k_{inact} was achieved, while the electrophilicity of the warhead remained unchanged. Finally, we have developed irreversible inhibitors of PI3Kα (**19** and **22**) with rapid and covalent bond formation and higher cellular potency compared to CNX-1351.[27] X-ray crystallography confirmed the covalent bond formation between the cysteine thiol and the acrylamide. This specificity for Cys862 in PI3Kα was confirmed by NanoBRET assays. Compounds **19** and **22** showed excellent stability in rat liver microsomes compared to CNX-1351, highlighting the use of the described approach to design metabolically stable warheads and linkers, and to properly direct the electrophiles to remote cysteines. Consid-

ering the importance of PI3Kα as a target in oncology and vascular malformations, irreversible PI3Kα inhibitors could provide highly specific, long-acting, on-target therapeutics with unprecedented pharmacological properties.

The presented workflow, including a stepwise optimization of proximity and metabolic stability, can serve as a template to target distal cysteines across the kinome, accelerating the characterization of the role of different kinases in human disease.

METHODS

Compounds Synthesis and Characterization. All final compounds were synthesized in a purity ≥95% (see the Supporting Information for synthetic procedures).^{1}H,^{19}F, and ^{13}C NMR spectra were recorded on a Bruker Avance 400 spectrometer. NMR spectra were obtained in deuterated solvents, namely, CDCl$_3$ or (CD$_3$)$_2$SO. The chemical shift (δ values) are reported in ppm and corrected to the signal of the deuterated solvents [7.26 ppm (^{1}H NMR) and 77.16 ppm (^{13}C NMR) for CDCl$_3$; and 2.50 ppm (^{1}H NMR) and 39.52 ppm (^{13}C NMR) for (CD$_3$)$_2$SO].^{19}F NMR spectra are calibrated relative to CFCl$_3$ (δ = 0 ppm) as external standard (see the Supporting Information).

Determination of k_{chem} Using β-Mercaptoethanol (βME). The tested compounds (1 mM) were reacted with indicated concentrations of βME (Tables S2, S3, and S5) at 37 °C in a 4:1 DMSO/PBS (pH 7.4) mixture. The loss of inhibitor and formation of inhibitor-βME adduct was monitored by HPLC (Ultimate 3000SD System, ThermoFisher) at 20 min to 1 h intervals depending on reaction rates. Inhibitor-βME adduct was identified by MALDI-ToF MS (Voyager-DeTM Pro measured in m/z; see the MALDI-MS Spectra of β-Mercaptoethanol Adducts section in the Supporting Information). The experiments were performed in triplicate. For further details, see the Supporting Information.

Structure Modeling of PI3K and mTOR Kinase Complexes. The coordinates of PQR530 in PI3Kα (PDB ID 6OAC)[59] were used as starting points to dock molecules into the ATP-binding sites. Ligands in crystal structures were manually docked using Maestro 11.1 and energy minimization was subsequently carried out. Further measurements and figures were generated in Maestro 11.1 and Chimera UCSF.

Determination of Inhibitor Binding by TR-FRET. TR-FRET was performed by a LanthaScreen Technology (Life Technologies) assay as described in ref 42. In brief, displacement of AlexaFluor647-labeled Kinase Tracer 314 (#PV6087, K_d of 2.2 nM for PI3Kα) from a kinase/antibody/tracer (KAT) complex induced by the addition of increasing inhibitor concentrations was measured. The KAT was premixed in PI3Kα assay buffer composed of 50 mM HEPES pH 7.5, 10 mM MgCl$_2$, 1 mM ethylene glycol-bis(β-aminoethyl ether)-N,N,N′,N′-tetraacetic acid (EGTA), and 0.01% (v/v) Brij-35 from recombinant N-terminally (His)$_6$-tagged PI3Kα [(His)$_6$-p110α/p85α complex, 5 nM, #PV4789], biotinylated anti-(His)$_6$-tag antibody (2 nM, #PV6089), and LanthaScreen Eu-steptavidin (2 nM, #PV5899) as well as the AlexaFluor647-labeled Kinase Tracer 314 (20 nM). Rapid dispensing of inhibitors was performed on an I.DOT One dispenser (Dispendix). For experimental details and data analysis, refer to the Supporting Information.

Determination of Inhibitor Dissociation and Kinetic Constants. Dissociation constants (K_i) and the rate of covalent bond formation (k_{inact}) for PI3Kα were determined by LanthaScreen Technology as above, and fluorescence changes were recorded as a function of time and inhibitor concentration. Recordings were started immediately after compound addition and continued at 60 s intervals for 1.5 h. FRET emission ratios were calculated by dividing blank-corrected FRET acceptor signals (AlexaFluor647-labeled Tracer 314, 665 nm) by donor signals (Eu-labeled steptavidin, 620 nm). Kinetic parameters (K_i and k_{inact}) were obtained through the global fitting of time- and concentration-dependent FRET ratios using KinTek Global Kinetic Explorer software,[73,74] with adaptions to fit enzymatic covalent reaction data as previously described.[75,76] For details on the experimental setup and data analysis, see the Supporting Information.

KinTek Modeling of On-/Off-Target Reactions. The reaction progression curves of on-/off-target covalent binding for each inhibitor were modeled using KinTek Kinetic software.[73,74] The underlying enzymatic reaction mechanism is detailed in the Supporting Information.

Stochastic Approach to Calculation of Covalent Reaction Rates. The details of covalent binding reaction models and the derivation of stochastic and macroscopic equations are explained in detail in the Supporting Information.

Protein Mass Spectrometry. Details on samples preparation are reported in the Supporting Information. LC-MS/MS data were acquired in data-dependent mode on a system consisting of a Proxeon Ultra easy LC and an Orbitrap Elite (Thermo). Peptides were identified using the Trans-Proteomic-Pipeline (TPP) v5.1 with the search engine Myrimatch and the parameters: precursor tolerance: 10 ppm; fragment tolerance: 0.5 Da; dynamic modifications: iodoacetamide (C), oxidation (M); **19** (C), **22** (C) and **22r** (C), enzyme: trypsin; missed cleavages: 2. Peptide probabilities were assigned with PeptideProphet and iProphet and the dataset was filtered with a peptide probability (iprobability) of 0.9. MS1 XIC traces of the Cys862-containing peptides with different covalent modifications were extracted using Skyline v4.2. The conversion rate of Cys862 through the compounds was quantified using LC-SRM.

Purification of PI3Kα Protein for Structural Studies. PI3Kα (ΔABD-LBS p110α 105−1048) was expressed by recombinant baculovirus in Sf9 cells, purified, and initially crystallized as previously published.[59,77] Additional details are provided in the Supporting Information.

Crystallography. For co-crystallization of **19** and **22**, protein at 5.8 mg/mL was initially incubated for 20 h on ice with a 2-fold molar excess of inhibitor. Crystals collected for diffraction were obtained from 1 μL hanging drops containing 0.5 μL of inhibitor-bound protein mixed with 0.4 μL reservoir (6−10% poly(ethylene glycol) (PEG)6000, 0.6 M sodium formate, 0.1 M N-cyclohexyl-2-aminoethanesulfonic acid (CHES) pH 9.5, 5 mM tris(2-carboxyethyl)phosphine (TCEP) pH 7.5) and 0.1 μL of 1/1000 diluted micro-seeds crushed from a drop of the original apo crystals. Diffraction data for PI3K crystals were collected at beamline 08ID-1 of the Canadian Light Source (**19** and **22**). Data were collected at 12.670 keV (CLS) for **19** and **22**. For details on the experimental setup, data analysis, and full data collection details, see the Supporting Information.

NanoBRET Target Engagement Assay. To investigate drug-target engagement on a cellular level, HEK293 cells were transiently transfected (using jetPEI from Polyplus-transfection, #101B-010N) with expression plasmids for nano-luciferase (NanoLuc) fused to the N-termini of the catalytic PI3K subunits p110α, p110α Cys862Ser, p110β, and p110δ (Promega #CS1810C52, #CS1810C250, #CS1810C390, and #CS1810C246) in combination with a vector for the regulatory p85α subunit. Transfected cells were seeded to 96-well assay plates (Falcon, #359296) in Opti-MEM I medium without phenol red (Gibco, #11058021) and exposed to inhibitors (3 μM) for 2 h (37 °C, 5% CO₂). Inhibitors were then removed, and cells were washed twice with medium (10 min intervals, each). Finally, energy transfer probe (Tracer 03, Promega, # N260B), NanoGlo Substrate (Promega, #N157C), and extracellular NanoLuc inhibitor (Promega, #N235B) were added as detailed in the Supporting Information, before donor and acceptor luminescences were recorded on a Berthold Mithras² LB943 luminometer equipped with 460 ± 35 nm BP (donor) and 600 nm LP (acceptor) filters (integration time set to 0.5 s). To generate raw BRET ratio values, the acceptor emission intensity (618 nm) was divided by the donor emission intensity (460 nm). Background correction was performed by subtracting the BRET ratio in the absence of tracer (average of no tracer control) from the BRET ratio of each sample.

Determination of Cellular PKB/Akt Phosphorylation. For in-cell western (ICW) assays, 1.2 × 10⁴ SKOV3 cells in DMEM (Sigma, D-5671) supplemented with 10% heat-inactivated fetal calf serum (FCS), L-glutamine (2 mM), and 1% penicillin−streptomycin were seeded into 96-well plates (Cell Carrier, PerkinElmer, #6005550) and pre-incubated for 18 h (37 °C, 5% CO₂). Inhibitors (2 mM stock solutions in DMSO) were added using an I.DOT One dispenser

(Dispendix) to generate a concentration range of 0.8 nM to 3 μM (11 intervals) in 0.05% DMSO per plate. Samples were incubated for 1 h (37 °C, 5% CO₂), fixed (4% paraformaldehyde [PFA] in PBS for 30 min at RT), blocked and permeabilized (1% bovine serum albumin [BSA], 0.1% Triton X-100, 5% goat serum in PBS, 30 min at RT), and co-stained with rabbit monoclonal anti-phospho-Ser473 PKB/Akt (Cell Signaling Technology, #4058) and mouse anti-α-tubulin (Sigma, # T9026) antibodies. The following day, primary antibodies were removed by washes with PBS (1% BSA, 0.1% Triton X-100), and secondary antibodies (IRDye680-conjugated goat anti-mouse, and IRDye800-conjugated goat anti-rabbit antibodies) were added for 90 min (LICOR #926-68070 and #926-32211, shaking, RT, in the dark). After removal of secondary antibodies, fluorescence was finally recorded on an Odyssey CLx infrared imaging scanner (LICOR) and the ratio of pPKB (800 nm) over α-tubulin (680 nm) was determined, as further described in ref 42 and the Supporting Information.

In-Cell Western (ICW) Washout Experiments. For ICW assays with timed removal of inhibitor (so-called "washout" experiments), 1.2 × 10⁴ SKOV3, 1.6 × 10⁴ MCF7, or 1.4 × 10⁴ T47D cells (propagated as indicated above) were seeded per well of a 96-well assay plate (Cell Carrier; PerkinElmer, #6005550) and incubated for 40 h (37 °C, 5% CO₂). Inhibitor stock solutions (2 mM in DMSO) were diluted to 60 μM working solutions in DMEM medium (with 10% FCS, see above) and added to a final concentration of 3 μM (max. 0.15% DMSO) per well. After inhibitor addition, the cells were incubated for 2 h, then washed twice with medium to remove free inhibitors, and further incubated for the indicated times (37 °C, 5% CO₂). Values at t = 0 represent the measurement in the presence of inhibitors (no washout). Where indicated, TGX221 was added (3 μM, 1 h prior to fixation) to probe for cell-line-dependent, PI3Kβ-derived contributions to pPKB/Akt formation. Finally, the cells were fixed, blocked, permeabilized, and stained for fluorescence detection as described above.

Metabolic Stability in Rat Liver Microsomes. The assay was performed using Sprague Dawley rat liver microsomes at 0.5 mg/mL. Details on the experimental setup are reported in the Supporting Information. The experiment was initiated by the addition of 70 μL of a 10 mM NADPH solution in phosphate buffer (100 mM, pH 7.4, supplemented with 2 mM MgCl₂) to the prewarmed (37 °C) microsomes/buffer/test item mix. Samples (70 μL) were removed from the incubations after 0, 10, 30, and 60 min and transferred to the quenching plate for sample preparation containing acetonitrile (ACN) supplemented with the internal standards. The experimental test item incubations were run in duplicate (n = 2). Verapamil was used as a high-clearance positive control (n = 2) to demonstrate the microsomal CYP enzyme activity. For quantitative analysis of test and reference items, LC-MS systems were used (see the Supporting Information).

■ ASSOCIATED CONTENT

Ⓢ Supporting Information

The Supporting Information is available free of charge at https://pubs.acs.org/doi/10.1021/jacs.1c13568.

Comparison of PI3Kα X-ray crystallographic complexes (Table S1); reaction rate constants (Table S2); KinTek modeling (Figure S1); time- and concentration-dependent TR-FRET data and time-dependent IC₅₀ shift calculations (Figures S2 and S4); summary data (Tables S3 and S5); modeling into PI3Kα (Figures S3 and S5); estimation of reactive volume (Vᵣ) and local concentration of warhead (Table S4); CovDock Schrödinger modeling (Figure S6); k_chem/k_inact ratio vs reactive volume relations (Figure S7); calculation of σ factors (Table S6); protein mass spectrometry (Figure S8); summary of compound-modified peptides (Table S7); MS/MS spectra (Figure S9); data collection and refinement statistics (molecular replacement, Table S8); NanoBRET experiments with CNX-1351 (Figure S10); lipophilic efficiency (Table S9); metabolic stability (Table S10);

affinities to PI3K and PI3K-related kinases (PIKK, Table S11); TREEspot data visualization of KINOMEScan interactions (Figure S11); selectivity profile (Table S12); protein kinase interactions (KINOMEscan data, Table S13); time- and concentration-dependent TR-FRET determination of IC50s (Figures S12 and S13); comparison of chemical structures (Figure S14); synthetic Schemes S1−S3; detailed experimental procedures; synthesis and characterization of intermediates and final compounds; ^{1}H NMR, ^{13}C{^{1}H} NMR, MALDI-MS, and high-resolution mass spectrometry (HRMS) spectra; HPLC chromatograms; MALDI-MS spectra of β-mercaptoethanol adducts; chemical structures of final compounds, intermediates, and reference compounds; KinTek global kinetic explorer data fitting of TR-FRET traces; and chemical structures of final compounds, intermediates, and reference compounds (PDF)

Proteomics data set file: peptide probabilities assigned with PeptideProphet and iProphet, MS1 XIC traces of the Cys862-containing peptides with different covalent modifications extracted using Skyline v4.2 (XLSX)

Accession Codes

The coordinates of compounds **19** and **22** covalently bound to the PI3Kα catalytic subunit p110α have been deposited at www.pdb.org and www.rcsb.org with PDB ID code 7R9V and 7R9Y, respectively.

■ AUTHOR INFORMATION

Corresponding Author

Matthias P. Wymann − *Department of Biomedicine, University of Basel, 4058 Basel, Switzerland;* ⓘ orcid.org/0000-0003-3349-4281; Phone: +41 61 207 5046; Email: matthias.wymann@unibas.ch; Fax: +41 61 207 3566

Authors

Chiara Borsari − *Department of Biomedicine, University of Basel, 4058 Basel, Switzerland;* ⓘ orcid.org/0000-0002-4688-8362

Erhan Keles − *Department of Biomedicine, University of Basel, 4058 Basel, Switzerland*

Jacob A. McPhail − *Department of Biochemistry and Microbiology, University of Victoria, Victoria, British Columbia V8W 2Y2, Canada*

Alexander Schaefer − *Department of Biology, Institute of Molecular Systems Biology, ETH Zurich, 8093 Zürich, Switzerland*

Rohitha Sriramaratnam − *Department of Biomedicine, University of Basel, 4058 Basel, Switzerland*

Wojciech Goch − *Department of Physical Chemistry, Faculty of Pharmacy, Medical University of Warsaw, 02-097 Warsaw, Poland*

Thorsten Schaefer − *Department of Biomedicine, University of Basel, 4058 Basel, Switzerland*

Martina De Pascale − *Department of Biomedicine, University of Basel, 4058 Basel, Switzerland;* ⓘ orcid.org/0000-0002-7546-2766

Wojciech Bal − *Institute of Biochemistry and Biophysics, Polish Academy of Sciences, 02-106 Warsaw, Poland;* ⓘ orcid.org/0000-0003-3780-083X

Matthias Gstaiger − *Department of Biology, Institute of Molecular Systems Biology, ETH Zurich, 8093 Zürich, Switzerland*

John E. Burke − *Department of Biochemistry and Microbiology, University of Victoria, Victoria, British Columbia V8W 2Y2, Canada;* ⓘ orcid.org/0000-0001-7904-9859

Complete contact information is available at:
https://pubs.acs.org/10.1021/jacs.1c13568

Author Contributions

[#]C.B. and E.K. contributed equally to this work. The manuscript was written through contributions of all authors. All authors have given approval to the final version of the manuscript.

Notes

The authors declare no competing financial interest.

■ ACKNOWLEDGMENTS

■ REFERENCES

(1) Miller, V. A.; Hirsh, V.; Cadranel, J.; Chen, Y.-M.; Park, K.; Kim, S.-W.; Zhou, C.; Su, W.-C.; Wang, M.; Sun, Y.; Heo, D. S.; Crino, L.; Tan, E.-H.; Chao, T.-Y.; Shahidi, M.; Cong, X. J.; Lorence, R. M.; Yang, J. C.-H. Afatinib versus placebo for patients with advanced, metastatic non-small-cell lung cancer after failure of erlotinib, gefitinib, or both, and one or two lines of chemotherapy (LUX-Lung 1): a phase 2b/3 randomised trial. *Lancet Oncol.* **2012**, *13*, 528−538.

(2) Pan, Z.; Scheerens, H.; Li, S.-J.; Schultz, B. E.; Sprengeler, P. A.; Burrill, L. C.; Mendonca, R. V.; Sweeney, M. D.; Scott, K. C. K.; Grothaus, P. G.; Jeffery, D. A.; Spoerke, J. M.; Honigberg, L. A.; Young, P. R.; Dalrymple, S. A.; Palmer, J. T. Discovery of Selective Irreversible Inhibitors for Bruton's Tyrosine Kinase. *ChemMedChem* **2007**, *2*, 58−61.

(3) Yver, A. Osimertinib (AZD9291)—a science-driven, collaborative approach to rapid drug design and development. *Ann. Oncol.* **2016**, *27*, 1165−1170.

(4) Miles, J.; White, Y. Neratinib for the Treatment of Early-Stage HER2-Positive Breast Cancer. *J. Adv. Pract. Oncol.* **2018**, *9*, 750−754.

(5) Lau, S. C. M.; Batra, U.; Mok, T. S. K.; Loong, H. H. Dacomitinib in the Management of Advanced Non-Small-Cell Lung Cancer. *Drugs* **2019**, *79*, 823−831.

(6) Davids, M. S. Acalabrutinib for the initial treatment of chronic lymphocytic leukaemia. *Lancet* **2020**, *395*, 1234−1236.

(7) Guo, Y.; Liu, Y.; Hu, N.; Yu, D.; Zhou, C.; Shi, G.; Zhang, B.; Wei, M.; Liu, J.; Luo, L.; Tang, Z.; Song, H.; Guo, Y.; Liu, X.; Su, D.; Zhang, S.; Song, X.; Zhou, X.; Hong, Y.; Chen, S.; Cheng, Z.; Young, S.; Wei, Q.; Wang, H.; Wang, Q.; Lv, L.; Wang, F.; Xu, H.; Sun, H.; Xing, H.; Li, N.; Zhang, W.; Wang, Z.; Liu, G.; Sun, Z.; Zhou, D.; Li, W.; Liu, L.;

Wang, L.; Wang, Z. Discovery of Zanubrutinib (BGB-3111), a Novel, Potent, and Selective Covalent Inhibitor of Bruton's Tyrosine Kinase. *J. Med. Chem.* **2019**, *62*, 7923−7940.

(8) Roskoski, R., Jr. Properties of FDA-approved small molecule protein kinase inhibitors: A 2022 update. *Pharmacol. Res.* **2022**, *175*, No. 106037.

(9) Riely, G. J.; Neal, J. W.; Camidge, D. R.; Spira, A. I.; Piotrowska, Z.; Costa, D. B.; Tsao, A. S.; Patel, J. D.; Gadgeel, S. M.; Bazhenova, L.; Zhu, V. W.; West, H. L.; Mekhail, T.; Gentzler, R. D.; Nguyen, D.; Vincent, S.; Zhang, S.; Lin, J.; Bunn, V.; Jin, S.; Li, S.; Jänne, P. A. Activity and Safety of Mobocertinib (TAK-788) in Previously Treated Non-Small Cell Lung Cancer with EGFR Exon 20 Insertion Mutations from a Phase I/II Trial. *Cancer Discovery* **2021**, *11*, 1688−1699.

(10) Singh, J.; Petter, R. C.; Baillie, T. A.; Whitty, A. The resurgence of covalent drugs. *Nat. Rev. Drug Discovery* **2011**, *10*, 307−317.

(11) London, N.; Miller, R. M.; Krishnan, S.; Uchida, K.; Irwin, J. J.; Eidam, O.; Gibold, L.; Cimermančič, P.; Bonnet, R.; Shoichet, B. K.; Taunton, J. Covalent docking of large libraries for the discovery of chemical probes. *Nat. Chem. Biol.* **2014**, *10*, 1066−1072.

(12) Zhao, Z.; Liu, Q.; Bliven, S.; Xie, L.; Bourne, P. E. Determining Cysteines Available for Covalent Inhibition Across the Human Kinome. *J. Med. Chem.* **2017**, *60*, 2879−2889.

(13) Liu, Q.; Sabnis, Y.; Zhao, Z.; Zhang, T.; Buhrlage, S. J.; Jones, L. H.; Gray, N. S. Developing irreversible inhibitors of the protein kinase cysteinome. *Chem. Biol.* **2013**, *20*, 146−159.

(14) Barf, T.; Covey, T.; Izumi, R.; van de Kar, B.; Gulrajani, M.; van Lith, B.; van Hoek, M.; de Zwart, E.; Mittag, D.; Demont, D.; Verkaik, S.; Krantz, F.; Pearson, P. G.; Ulrich, R.; Kaptein, A. Acalabrutinib (ACP-196): A Covalent Bruton Tyrosine Kinase Inhibitor with a Differentiated Selectivity and In Vivo Potency Profile. *J. Pharmacol. Exp. Ther.* **2017**, *363*, 240−252.

(15) Cheng, H.; Planken, S. Precedence and Promise of Covalent Inhibitors of EGFR and KRAS for Patients with Non-Small-Cell Lung Cancer. *ACS Med. Chem. Lett.* **2018**, *9*, 861−863.

(16) Tomassi, S.; Lategahn, J.; Engel, J.; Keul, M.; Tumbrink, H. L.; Ketzer, J.; Mühlenberg, T.; Baumann, M.; Schultz-Fademrecht, C.; Bauer, S.; Rauh, D. Indazole-Based Covalent Inhibitors To Target Drug-Resistant Epidermal Growth Factor Receptor. *J. Med. Chem.* **2017**, *60*, 2361−2372.

(17) Planken, S.; Behenna, D. C.; Nair, S. K.; Johnson, T. O.; Nagata, A.; Almaden, C.; Bailey, S.; Ballard, T. E.; Bernier, L.; Cheng, H.; Cho-Schultz, S.; Dalvie, D.; Deal, J. G.; Dinh, D. M.; Edwards, M. P.; Ferre, R. A.; Gajiwala, K. S.; Hemkens, M.; Kania, R. S.; Kath, J. C.; Matthews, J.; Murray, B. W.; Niessen, S.; Orr, S. T.; Pairish, M.; Sach, N. W.; Shen, H.; Shi, M.; Solowiej, J.; Tran, K.; Tseng, E.; Vicini, P.; Wang, Y.; Weinrich, S. L.; Zhou, R.; Zientek, M.; Liu, L.; Luo, Y.; Xin, S.; Zhang, C.; Lafontaine, J. Discovery of N-((3R,4R)-4-Fluoro-1-(6-((3-methoxy-1-methyl-1H-pyrazol-4-yl)amino)-9-methyl-9H-purin-2-yl)-pyrrolidine-3-yl)acrylamide (PF-06747775) through Structure-Based Drug Design: A High Affinity Irreversible Inhibitor Targeting Oncogenic EGFR Mutants with Selectivity over Wild-Type EGFR. *J. Med. Chem.* **2017**, *60*, 3002−3019.

(18) Zapf, C. W.; Gerstenberger, B. S.; Xing, L.; Limburg, D. C.; Anderson, D. R.; Caspers, N.; Han, S.; Aulabaugh, A.; Kurumbail, R.; Shakya, S.; Li, X.; Spaulding, V.; Czerwinski, R. M.; Seth, N.; Medley, Q. G. Covalent inhibitors of interleukin-2 inducible T cell kinase (itk) with nanomolar potency in a whole-blood assay. *J. Med. Chem.* **2012**, *55*, 10047−10063.

(19) Ward, R. A.; Colclough, N.; Challinor, M.; Debreczeni, J. E.; Eckersley, K.; Fairley, G.; Feron, L.; Flemington, V.; Graham, M. A.; Greenwood, R.; Hopcroft, P.; Howard, T. D.; James, M.; Jones, C. D.; Jones, C. R.; Renshaw, J.; Roberts, K.; Snow, L.; Tonge, M.; Yeung, K. Structure-Guided Design of Highly Selective and Potent Covalent Inhibitors of ERK1/2. *J. Med. Chem.* **2015**, *58*, 4790−4801.

(20) Angst, D.; Gessier, F.; Janser, P.; Vulpetti, A.; Wälchli, R.; Beerli, C.; Littlewood-Evans, A.; Dawson, J.; Nuesslein-Hildesheim, B.; Wieczorek, G.; Gutmann, S.; Scheufler, C.; Hinniger, A.; Zimmerlin, A.; Funhoff, E. G.; Pulz, R.; Cenni, B. Discovery of LOU064 (Remibrutinib), a Potent and Highly Selective Covalent Inhibitor of Bruton's Tyrosine Kinase. *J. Med. Chem.* **2020**, *63*, 5102−5118.

(21) Gurbani, D.; Du, G.; Henning, N. J.; Rao, S.; Bera, A. K.; Zhang, T.; Gray, N. S.; Westover, K. D. Structure and Characterization of a Covalent Inhibitor of Src Kinase. *Front. Mol. Biosci.* **2020**, *7*, No. 81.

(22) Abdeldayem, A.; Raouf, Y. S.; Constantinescu, S. N.; Moriggl, R.; Gunning, P. T. Advances in covalent kinase inhibitors. *Chem. Soc. Rev.* **2020**, *49*, 2617−2687.

(23) Yan, G.; Zhong, X.; Pu, C.; Yue, L.; Shan, H.; Lan, S.; Zhou, M.; Hou, X.; Yang, J.; Li, D.; Fan, S.; Li, R. Targeting Cysteine Located Outside the Active Site: An Effective Strategy for Covalent ALKi Design. *J. Med. Chem.* **2021**, *64*, 1558−1569.

(24) Jiang, B.; Jiang, J.; Kaltheuner, I. H.; Iniguez, A. B.; Anand, K.; Ferguson, F. M.; Ficarro, S. B.; Seong, B. K. A.; Greifenberg, A. K.; Dust, S.; Kwiatkowski, N. P.; Marto, J. A.; Stegmaier, K.; Zhang, T.; Geyer, M.; Gray, N. S. Structure-activity relationship study of THZ531 derivatives enables the discovery of BSJ-01-175 as a dual CDK12/13 covalent inhibitor with efficacy in Ewing sarcoma. *Eur. J. Med. Chem.* **2021**, *221*, No. 113481.

(25) Zhang, T.; Kwiatkowski, N.; Olson, C. M.; Dixon-Clarke, S. E.; Abraham, B. J.; Greifenberg, A. K.; Ficarro, S. B.; Elkins, J. M.; Liang, Y.; Hannett, N. M.; Manz, T.; Hao, M.; Bartkowiak, B.; Greenleaf, A. L.; Marto, J. A.; Geyer, M.; Bullock, A. N.; Young, R. A.; Gray, N. S. Covalent targeting of remote cysteine residues to develop CDK12 and CDK13 inhibitors. *Nat. Chem. Biol.* **2016**, *12*, 876−884.

(26) Kwiatkowski, N.; Zhang, T.; Rahl, P. B.; Abraham, B. J.; Reddy, J.; Ficarro, S. B.; Dastur, A.; Amzallag, A.; Ramaswamy, S.; Tesar, B.; Jenkins, C. E.; Hannett, N. M.; McMillin, D.; Sanda, T.; Sim, T.; Kim, N. D.; Look, T.; Mitsiades, C. S.; Weng, A. P.; Brown, J. R.; Benes, C. H.; Marto, J. A.; Young, R. A.; Gray, N. S. Targeting transcription regulation in cancer with a covalent CDK7 inhibitor. *Nature* **2014**, *511*, 616−620.

(27) Nacht, M.; Qiao, L.; Sheets, M. P.; St Martin, T.; Labenski, M.; Mazdiyasni, H.; Karp, R.; Zhu, Z.; Chaturvedi, P.; Bhavsar, D.; Niu, D.; Westlin, W.; Petter, R. C.; Medikonda, A. P.; Singh, J. Discovery of a Potent and Isoform-Selective Targeted Covalent Inhibitor of the Lipid Kinase PI3Kα. *J. Med. Chem.* **2013**, *56*, 712−721.

(28) Wymann, M. P.; Schneiter, R. Lipid signalling in disease. *Nat. Rev. Mol. Cell Biol.* **2008**, *9*, 162−176.

(29) Fruman, D. A.; Rommel, C. PI3K and cancer: lessons, challenges and opportunities. *Nat. Rev. Drug Discovery* **2014**, *13*, 140−156.

(30) Samuels, Y.; Wang, Z.; Bardelli, A.; Silliman, N.; Ptak, J.; Szabo, S.; Yan, H.; Gazdar, A.; Powell, S. M.; Riggins, G. J.; Willson, J. K.; Markowitz, S.; Kinzler, K. W.; Vogelstein, B.; Velculescu, V. E. High frequency of mutations of the PIK3CA gene in human cancers. *Science* **2004**, *304*, 554.

(31) Vanhaesebroeck, B.; Perry, M. W. D.; Brown, J. R.; André, F.; Okkenhaug, K. PI3K inhibitors are finally coming of age. *Nat. Rev. Drug Discovery* **2021**, *20*, 741−769.

(32) Yang, J.; Nie, J.; Ma, X.; Wei, Y.; Peng, Y.; Wei, X. Targeting PI3K in cancer: mechanisms and advances in clinical trials. *Mol. Cancer* **2019**, *18*, No. 26.

(33) Massacesi, C.; Di Tomaso, E.; Urban, P.; Germa, C.; Quadt, C.; Trandafir, L.; Aimone, P.; Fretault, N.; Dharan, B.; Tavorath, R.; Hirawat, S. PI3K inhibitors as new cancer therapeutics: implications for clinical trial design. *OncoTargets Ther.* **2016**, *9*, 203−210.

(34) Mishra, R.; Patel, H.; Alanazi, S.; Kilroy, M. K.; Garrett, J. T. PI3K Inhibitors in Cancer: Clinical Implications and Adverse Effects. *Int. J. Mol. Sci.* **2021**, *22*, No. 3464.

(35) Fritsch, C.; Huang, A.; Chatenay-Rivauday, C.; Schnell, C.; Reddy, A.; Liu, M.; Kauffmann, A.; Guthy, D.; Erdmann, D.; De Pover, A.; Furet, P.; Gao, H.; Ferretti, S.; Wang, Y.; Trappe, J.; Brachmann, S. M.; Maira, S. M.; Wilson, C.; Boehm, M.; Garcia-Echeverria, C.; Chene, P.; Wiesmann, M.; Cozens, R.; Lehar, J.; Schlegel, R.; Caravatti, G.; Hofmann, F.; Sellers, W. R. Characterization of the novel and specific PI3Kα inhibitor NVP-BYL719 and development of the patient stratification strategy for clinical trials. *Mol. Cancer Ther.* **2014**, *13*, 1117−1129.

(36) Markham, A. Alpelisib: First Global Approval. *Drugs* **2019**, *79*, 1249−1253.

(37) Narayan, P.; Prowell, T. M.; Gao, J. J.; Fernandes, L. L.; Li, E.; Jiang, X.; Qiu, J.; Fan, J.; Song, P.; Yu, J.; Zhang, X.; King-Kallimanis, B. L.; Chen, W.; Ricks, T. K.; Gong, Y.; Wang, X.; Windsor, K.; Rhieu, S. Y.; Geiser, G.; Banerjee, A.; Chen, X.; Reyes Turcu, F.; Chatterjee, D. K.; Pathak, A.; Seidman, J.; Ghosh, S.; Philip, R.; Goldberg, K. B.; Kluetz, P. G.; Tang, S.; Amiri-Kordestani, L.; Theoret, M. R.; Pazdur, R.; Beaver, J. A. FDA Approval Summary: Alpelisib Plus Fulvestrant for Patients with HR-positive, HER2-negative, PIK3CA-mutated, Advanced or Metastatic Breast Cancer. *Clin. Cancer Res.* **2021**, *27*, 1842−1849.

(38) André, F.; Ciruelos, E. M.; Juric, D.; Loibl, S.; Campone, M.; Mayer, I. A.; Rubovszky, G.; Yamashita, T.; Kaufman, B.; Lu, Y. S.; Inoue, K.; Pápai, Z.; Takahashi, M.; Ghaznawi, F.; Mills, D.; Kaper, M.; Miller, M.; Conte, P. F.; Iwata, H.; Rugo, H. S. Alpelisib plus fulvestrant for PIK3CA-mutated, hormone receptor-positive, human epidermal growth factor receptor-2-negative advanced breast cancer: final overall survival results from SOLAR-1. *Ann. Oncol.* **2021**, *32*, 208−217.

(39) Turner, S.; Chia, S.; Kanakamedala, H.; Hsu, W. C.; Park, J.; Chandiwana, D.; Ridolfi, A.; Yu, C. L.; Zarate, J. P.; Rugo, H. S. Effectiveness of Alpelisib + Fulvestrant Compared with Real-World Standard Treatment Among Patients with HR+, HER2-, PIK3CA-Mutated Breast Cancer. *Oncologist* **2021**, *26*, e1133−e1142.

(40) Verret, B.; Cortes, J.; Bachelot, T.; Andre, F.; Arnedos, M. Efficacy of PI3K inhibitors in advanced breast cancer. *Ann. Oncol.* **2019**, *30*, x12−x20.

(41) Venot, Q.; Blanc, T.; Rabia, S. H.; Berteloot, L.; Ladraa, S.; Duong, J. P.; Blanc, E.; Johnson, S. C.; Hoguin, C.; Boccara, O.; Sarnacki, S.; Boddaert, N.; Pannier, S.; Martinez, F.; Magassa, S.; Yamaguchi, J.; Knebelmann, B.; Merville, P.; Grenier, N.; Joly, D.; Cormier-Daire, V.; Michot, C.; Bole-Feysot, C.; Picard, A.; Soupre, V.; Lyonnet, S.; Sadoine, J.; Slimani, L.; Chaussain, C.; Laroche-Raynaud, C.; Guibaud, L.; Broissand, C.; Amiel, J.; Legendre, C.; Terzi, F.; Canaud, G. Targeted therapy in patients with PIK3CA-related overgrowth syndrome. *Nature* **2018**, *558*, 540−546.

(42) Bohnacker, T.; Prota, A. E.; Beaufils, F.; Burke, J. E.; Melone, A.; Inglis, A. J.; Rageot, D.; Sele, A. M.; Cmiljanovic, V.; Cmiljanovic, N.; Bargsten, K.; Aher, A.; Akhmanova, A.; Diaz, J. F.; Fabbro, D.; Zvelebil, M.; Williams, R. L.; Steinmetz, M. O.; Wymann, M. P. Deconvolution of Buparlisib's mechanism of action defines specific PI3K and tubulin inhibitors for therapeutic intervention. *Nat. Commun.* **2017**, *8*, No. 14683.

(43) Beaufils, F.; Cmiljanovic, N.; Cmiljanovic, V.; Bohnacker, T.; Melone, A.; Marone, R.; Jackson, E.; Zhang, X.; Sele, A.; Borsari, C.; Mestan, J.; Hebeisen, P.; Hillmann, P.; Giese, B.; Zvelebil, M.; Fabbro, D.; Williams, R. L.; Rageot, D.; Wymann, M. P. 5-(4,6-Dimorpholino-1,3,5-triazin-2-yl)-4-(trifluoromethyl)pyridin-2-amine (PQR309), a potent, brain-penetrant, orally bioavailable, pan-class I PI3K/mTOR inhibitor as clinical candidate in oncology. *J. Med. Chem.* **2017**, *60*, 7524−7538.

(44) Tarantelli, C.; Gaudio, E.; Arribas, A. J.; Kwee, I.; Hillmann, P.; Rinaldi, A.; Cascione, L.; Spriano, F.; Bernasconi, E.; Guidetti, F.; Carrassa, L.; Pittau, R. B.; Beaufils, F.; Ritschard, R.; Rageot, D.; Sele, A.; Dossena, B.; Rossi, F. M.; Zucchetto, A.; Taborelli, M.; Gattei, V.; Rossi, D.; Stathis, A.; Stussi, G.; Broggini, M.; Wymann, M. P.; Wicki, A.; Zucca, E.; Cmiljanovic, V.; Fabbro, D.; Bertoni, F. PQR309 is a novel dual PI3K/mTOR inhibitor with preclinical antitumor activity in lymphomas as a single agent and in combination therapy. *Clin. Cancer Res.* **2018**, *24*, 120−129.

(45) Wicki, A.; Brown, N.; Xyrafas, A.; Bize, V.; Hawle, H.; Berardi, S.; Cmiljanovic, N.; Cmiljanovic, V.; Stumm, M.; Dimitrijevic, S.; Herrmann, R.; Pretre, V.; Ritschard, R.; Tzankov, A.; Hess, V.; Childs, A.; Hierro, C.; Rodon, J.; Hess, D.; Joerger, M.; von Moos, R.; Sessa, C.; Kristeleit, R. First-in human, phase 1, dose-escalation pharmacokinetic and pharmacodynamic study of the oral dual PI3K and mTORC1/2 inhibitor PQR309 in patients with advanced solid tumors (SAKK 67/13). *Eur. J. Cancer* **2018**, *96*, 6−16.

(46) Borsari, C.; Rageot, D.; Beaufils, F.; Bohnacker, T.; Keles, E.; Buslov, I.; Melone, A.; Sele, A. M.; Hebeisen, P.; Fabbro, D.; Hillmann, P.; Wymann, M. P. Preclinical Development of PQR514, a Highly Potent PI3K Inhibitor Bearing a Difluoromethyl-Pyrimidine Moiety. *ACS Med. Chem. Lett.* **2019**, *10*, 1473−1479.

(47) Jackson, P. A.; Widen, J. C.; Harki, D. A.; Brummond, K. M. Covalent Modifiers: A Chemical Perspective on the Reactivity of α,β-Unsaturated Carbonyls with Thiols via Hetero-Michael Addition Reactions. *J. Med. Chem.* **2017**, *60*, 839−885.

(48) Flanagan, M. E.; Abramite, J. A.; Anderson, D. P.; Aulabaugh, A.; Dahal, U. P.; Gilbert, A. M.; Li, C.; Montgomery, J.; Oppenheimer, S. R.; Ryder, T.; Schuff, B. P.; Uccello, D. P.; Walker, G. S.; Wu, Y.; Brown, M. F.; Chen, J. M.; Hayward, M. M.; Noe, M. C.; Obach, R. S.; Philippe, L.; Shanmugasundaram, V.; Shapiro, M. J.; Starr, J.; Stroh, J.; Che, Y. Chemical and computational methods for the characterization of covalent reactive groups for the prospective design of irreversible inhibitors. *J. Med. Chem.* **2014**, *57*, 10072−10079.

(49) Martin, J. S.; MacKenzie, C. J.; Fletcher, D.; Gilbert, I. H. Characterising covalent warhead reactivity. *Bioorg. Med. Chem.* **2019**, *27*, 2066−2074.

(50) Lonsdale, R.; Burgess, J.; Colclough, N.; Davies, N. L.; Lenz, E. M.; Orton, A. L.; Ward, R. A. Expanding the Armory: Predicting and Tuning Covalent Warhead Reactivity. *J. Chem. Inf. Model.* **2017**, *57*, 3124−3137.

(51) Ma, S.; Devi-Kesavan, L. S.; Gao, J. Molecular dynamics simulations of the catalytic pathway of a cysteine protease: a combined QM/MM study of human cathepsin K. *J. Am. Chem. Soc.* **2007**, *129*, 13633−13645.

(52) Cusack, K. P.; Arnold, L. D.; Barberis, C. E.; Chen, H.; Ericsson, A. M.; Gaza-Bulseco, G. S.; Gordon, T. D.; Grinnell, C. M.; Harsch, A.; Pellegrini, M.; Tarcsa, E. A 13C NMR approach to categorizing potential limitations of alpha,beta-unsaturated carbonyl systems in drug-like molecules. *Bioorg. Med. Chem. Lett.* **2004**, *14*, 5503−5507.

(53) MacFaul, P. A.; Morley, A. D.; Crawford, J. J. A simple in vitro assay for assessing the reactivity of nitrile containing compounds. *Bioorg. Med. Chem. Lett.* **2009**, *19*, 1136−1138.

(54) Brameld, K. A.; Owens, T. D.; Verner, E.; Venetsanakos, E.; Bradshaw, J. M.; Phan, V. T.; Tam, D.; Leung, K.; Shu, J.; LaStant, J.; Loughhead, D. G.; Ton, T.; Karr, D. E.; Gerritsen, M. E.; Goldstein, D. M.; Funk, J. O. Discovery of the Irreversible Covalent FGFR Inhibitor 8-(3-(4-Acryloylpiperazin-1-yl)propyl)-6-(2,6-dichloro-3,5-dimethoxyphenyl)-2-(methylamino)pyrido[2,3-d]pyrimidin-7(8H)-one (PRN1371) for the Treatment of Solid Tumors. *J. Med. Chem.* **2017**, *60*, 6516−6527.

(55) Cee, V. J.; Volak, L. P.; Chen, Y.; Bartberger, M. D.; Tegley, C.; Arvedson, T.; McCarter, J.; Tasker, A. S.; Fotsch, C. Systematic Study of the Glutathione (GSH) Reactivity of N-Arylacrylamides: 1. Effects of Aryl Substitution. *J. Med. Chem.* **2015**, *58*, 9171−9178.

(56) Birkholz, A.; Kopecky, D. J.; Volak, L. P.; Bartberger, M. D.; Chen, Y.; Tegley, C. M.; Arvedson, T.; McCarter, J. D.; Fotsch, C.; Cee, V. J. Systematic Study of the Glutathione Reactivity of N-Phenyl-acrylamides: 2. Effects of Acrylamide Substitution. *J. Med. Chem.* **2020**, *63*, 11602−11614.

(57) Zhu, K.; Borrelli, K. W.; Greenwood, J. R.; Day, T.; Abel, R.; Farid, R. S.; Harder, E. Docking covalent inhibitors: a parameter free approach to pose prediction and scoring. *J. Chem. Inf. Model.* **2014**, *54*, 1932−1940.

(58) Toledo Warshaviak, D.; Golan, G.; Borrelli, K. W.; Zhu, K.; Kalid, O. Structure-based virtual screening approach for discovery of covalently bound ligands. *J. Chem. Inf. Model.* **2014**, *54*, 1941−1950.

(59) Rageot, D.; Bohnacker, T.; Keles, E.; McPhail, J. A.; Hoffmann, R. M.; Melone, A.; Borsari, C.; Sriramaratnam, R.; Sele, A. M.; Beaufils, F.; Hebeisen, P.; Fabbro, D.; Hillmann, P.; Burke, J. E.; Wymann, M. P. (S)-4-(Difluoromethyl)-5-(4-(3-methylmorpholino)-6-morpholino-1,3,5-triazin-2-yl)pyridin-2-amine (PQR530), a potent, orally bioavailable, and brain-penetrable dual inhibitor of class I PI3K and mTOR kinase. *J. Med. Chem.* **2019**, *62*, 6241−6261.

(60) Goel, P.; Alam, O.; Naim, M. J.; Nawaz, F.; Iqbal, M.; Alam, M. I. Recent advancement of piperidine moiety in treatment of cancer- A review. *Eur. J. Med. Chem.* **2018**, *157*, 480−502.

(61) Copeland, R. A. Evaluation of enzyme inhibitors in drug discovery. A guide for medicinal chemists and pharmacologists. *Methods Biochem. Anal.* **2005**, *46*, 1−265.

(62) Strelow, J. M. A Perspective on the Kinetics of Covalent and Irreversible Inhibition. *SLAS Discovery* **2017**, *22*, 3−20.

(63) Dale, N. C.; Johnstone, E. K. M.; White, C. W.; Pfleger, K. D. G. NanoBRET: The Bright Future of Proximity-Based Assays. *Front. Bioeng. Biotechnol.* **2019**, *7*, No. 56.

(64) Vasta, J. D.; Corona, C. R.; Wilkinson, J.; Zimprich, C. A.; Hartnett, J. R.; Ingold, M. R.; Zimmerman, K.; Machleidt, T.; Kirkland, T. A.; Huwiler, K. G.; Ohana, R. F.; Slater, M.; Otto, P.; Cong, M.; Wells, C. I.; Berger, B. T.; Hanke, T.; Glas, C.; Ding, K.; Drewry, D. H.; Huber, K. V. M.; Willson, T. M.; Knapp, S.; Muller, S.; Meisenheimer, P. L.; Fan, F.; Wood, K. V.; Robers, M. B. Quantitative, Wide-Spectrum Kinase Profiling in Live Cells for Assessing the Effect of Cellular ATP on Target Engagement. *Cell Chem. Biol.* **2018**, *25*, 206.e11−214.e11.

(65) Ikediobi, O. N.; Davies, H.; Bignell, G.; Edkins, S.; Stevens, C.; O'Meara, S.; Santarius, T.; Avis, T.; Barthorpe, S.; Brackenbury, L.; Buck, G.; Butler, A.; Clements, J.; Cole, J.; Dicks, E.; Forbes, S.; Gray, K.; Halliday, K.; Harrison, R.; Hills, K.; Hinton, J.; Hunter, C.; Jenkinson, A.; Jones, D.; Kosmidou, V.; Lugg, R.; Menzies, A.; Mironenko, T.; Parker, A.; Perry, J.; Raine, K.; Richardson, D.; Shepherd, R.; Small, A.; Smith, R.; Solomon, H.; Stephens, P.; Teague, J.; Tofts, C.; Varian, J.; Webb, T.; West, S.; Widaa, S.; Yates, A.; Reinhold, W.; Weinstein, J. N.; Stratton, M. R.; Futreal, P. A.; Wooster, R. Mutation analysis of 24 known cancer genes in the NCI-60 cell line set. *Mol. Cancer Ther.* **2006**, *5*, 2606−2612.

(66) Gall, V. A.; Philips, A. V.; Qiao, N.; Clise-Dwyer, K.; Perakis, A. A.; Zhang, M.; Clifton, G. T.; Sukhumalchandra, P.; Ma, Q.; Reddy, S. M.; Yu, D.; Molldrem, J. J.; Peoples, G. E.; Alatrash, G.; Mittendorf, E. A. Trastuzumab Increases HER2 Uptake and Cross-Presentation by Dendritic Cells. *Cancer Res.* **2017**, *77*, 5374−5383.

(67) Chaussade, C.; Rewcastle, G. W.; Kendall, J. D.; Denny, W. A.; Cho, K.; Grønning, L. M.; Chong, M. L.; Anagnostou, S. H.; Jackson, S. P.; Daniele, N.; Shepherd, P. R. Evidence for functional redundancy of class IA PI3K isoforms in insulin signalling. *Biochem. J.* **2007**, *404*, 449−458.

(68) Freeman-Cook, K. D.; Hoffman, R. L.; Johnson, T. W. Lipophilic efficiency: the most important efficiency metric in medicinal chemistry. *Future Med. Chem.* **2013**, *5*, 113−115.

(69) Leeson, P. D.; Springthorpe, B. The influence of drug-like concepts on decision-making in medicinal chemistry. *Nat. Rev. Drug Discovery* **2007**, *6*, 881−890.

(70) Chaikuad, A.; Koch, P.; Laufer, S. A.; Knapp, S. The Cysteinome of Protein Kinases as a Target in Drug Development. *Angew. Chem., Int. Ed.* **2018**, *57*, 4372−4385.

(71) Zhang, T.; Inesta-Vaquera, F.; Niepel, M.; Zhang, J.; Ficarro, S. B.; Machleidt, T.; Xie, T.; Marto, J. A.; Kim, N.; Sim, T.; Laughlin, J. D.; Park, H.; LoGrasso, P. V.; Patricelli, M.; Nomanbhoy, T. K.; Sorger, P. K.; Alessi, D. R.; Gray, N. S. Discovery of potent and selective covalent inhibitors of JNK. *Chem. Biol.* **2012**, *19*, 140−154.

(72) Zhang, T.; Hatcher, J. M.; Teng, M.; Gray, N. S.; Kostic, M. Recent Advances in Selective and Irreversible Covalent Ligand Development and Validation. *Cell Chem. Biol.* **2019**, *26*, 1486−1500.

(73) Johnson, K. A. Fitting enzyme kinetic data with KinTek Global Kinetic Explorer. *Computer Methods Part B*; Methods in Enzymology; Elsevier B.V., 2009; Vol. *467*, pp 601−626.

(74) Johnson, K. A.; Simpson, Z. B.; Blom, T. Global kinetic explorer: a new computer program for dynamic simulation and fitting of kinetic data. *Anal. Biochem.* **2009**, *387*, 20−29.

(75) Janes, M. R.; Zhang, J.; Li, L. S.; Hansen, R.; Peters, U.; Guo, X.; Chen, Y.; Babbar, A.; Firdaus, S. J.; Darjania, L.; Feng, J.; Chen, J. H.; Li, S.; Li, S.; Long, Y. O.; Thach, C.; Liu, Y.; Zarieh, A.; Ely, T.; Kucharski, J. M.; Kessler, L. V.; Wu, T.; Yu, K.; Wang, Y.; Yao, Y.; Deng, X.; Zarrinkar, P. P.; Brehmer, D.; Dhanak, D.; Lorenzi, M. V.; Hu-Lowe, D.; Patricelli, M. P.; Ren, P.; Liu, Y. Targeting KRAS Mutant Cancers with a Covalent G12C-Specific Inhibitor. *Cell* **2018**, *172*, 578.e17−589.e17.

(76) Müller, M. P.; Jeganathan, S.; Heidrich, A.; Campos, J.; Goody, R. S. Nucleotide based covalent inhibitors of KRas can only be efficient in vivo if they bind reversibly with GTP-like affinity. *Sci. Rep.* **2017**, *7*, No. 3687.

(77) Chen, P.; Deng, Y. L.; Bergqvist, S.; Falk, M. D.; Liu, W.; Timofeevski, S.; Brooun, A. Engineering of an isolated p110α subunit of PI3Kα permits crystallization and provides a platform for structure-based drug design. *Protein Sci.* **2014**, *23*, 1332−1340.

(78) Marcotte, D. J.; Liu, Y. T.; Arduini, R. M.; Hession, C. A.; Miatkowski, K.; Wildes, C. P.; Cullen, P. F.; Hong, V.; Hopkins, B. T.; Mertsching, E.; Jenkins, T. J.; Romanowski, M. J.; Baker, D. P.; Silvian, L. F. Structures of human Bruton's tyrosine kinase in active and inactive conformations suggest a mechanism of activation for TEC family kinases. *Protein Sci.* **2010**, *19*, 429−439.

(79) Gajiwala, K. S.; Feng, J.; Ferre, R.; Ryan, K.; Brodsky, O.; Weinrich, S.; Kath, J. C.; Stewart, A. Insights into the aberrant activity of mutant EGFR kinase domain and drug recognition. *Structure* **2013**, *21*, 209−219.

(80) Montero, D.; Tachibana, C.; Rahr Winther, J.; Appenzeller-Herzog, C. Intracellular glutathione pools are heterogeneously concentrated. *Redox Biol.* **2013**, *1*, 508−513.

(81) Choi, B.; Rempala, G. A.; Kim, J. K. Beyond the Michaelis-Menten equation: Accurate and efficient estimation of enzyme kinetic parameters. *Sci. Rep.* **2017**, *7*, No. 17018.

(82) Schwartz, P. A.; Kuzmic, P.; Solowiej, J.; Bergqvist, S.; Bolanos, B.; Almaden, C.; Nagata, A.; Ryan, K.; Feng, J.; Dalvie, D.; Kath, J. C.; Xu, M.; Wani, R.; Murray, B. W. Covalent EGFR inhibitor analysis reveals importance of reversible interactions to potency and mechanisms of drug resistance. *Proc. Natl. Acad. Sci. U.S.A.* **2014**, *111*, 173−178.

(83) Yu, C.; Miao, W.; Wang, J.; Hao, E.; Jiao, L. PyrrolylBODIPYs: Syntheses, Properties, and Application as Environment-Sensitive Fluorescence Probes. *ACS Omega* **2017**, *2*, 3551−3561.

⬛ Recommended by ACS